Journal of Hazardous Materials 473 (2024) 134686

Contents lists available at ScienceDirect

Journal of Hazardous Materials

journal homepage: www.elsevier.com/locate/jhazmat

Hazard assessment of hexagonal boron nitride and hexagonal boron nitride reinforced thermoplastic polyurethane composites using human skin and lung cells

Michela Carlin [a], Jasreen Kaur [b], Dinu Zinovie Ciobanu [c], Zhengmei Song [d], Magnus Olsson [b], Tiberiu Totu [e,f,g], Govind Gupta [e], Guotao Peng [b], Viviana Jehová González [h], Iwona Janica [d], Victor Fuster Pozo [e], Savvina Chortarea [e], Marija Buljan [e,f], Tina Buerki-Thurnherr [e], Antonio Esau del Rio Castillo [i], Sanjay B. Thorat [i], Francesco Bonaccorso [i], Aurelia Tubaro [a], Ester Vazquez [h,j], Maurizio Prato [k,l,m], Andrea Armirotti [c], Peter Wick [e], Alberto Bianco [d,*], Bengt Fadeel [b,*], Marco Pelin [a,*]

[a] Department of Life Sciences, University of Trieste, Trieste, Italy
[b] Institute of Environmental Medicine, Karolinska Institutet, Stockholm, Sweden
[c] Analytical Chemistry Facility, Italian Institute of Technology, Genoa, Italy
[d] CNRS, Immunology, Immunopathology and Therapeutic Chemistry, UPR3572, University of Strasbourg, ISIS, 67000 Strasbourg, France
[e] Laboratory for Particles-Biology Interactions, Federal Laboratory for Materials Science and Technology, (EMPA), St. Gallen, Switzerland
[f] Swiss Institute of Bioinformatics (SIB), Lausanne, Switzerland
[g] Department of Health Sciences and Technology, Eidgenössische Technische Hochschule Zürich (ETH), Zurich, Switzerland
[h] Regional Institute of Applied Scientific Research (IRICA), University of Castilla-La Mancha, Ciudad Real, Spain
[i] BeDimensional, Genoa, Italy
[j] Department of Organic Chemistry, Faculty of Science and Chemistry Technologies, University of Castilla-La Mancha, Ciudad Real, Spain
[k] Department of Chemical and Pharmaceutical Sciences, University of Trieste, Trieste, Italy
[l] Center for Cooperative Research in Biomaterials (CIC biomaGUNE), Basque Research and Technology Alliance (BRTA), Donostia-San Sebastian, Spain
[m] Basque Foundation for Science (IKERBASQUE), Bilbao, Spain

HIGHLIGHTS

- hBN, abraded hBN composite with TPU and relevant degraded products were studied.
- hBN and TPU-hBN did not induce significant cytotoxicity in HaCaT and BEAS-2B cells.
- Photochemical degradation of the materials did not induce significant cytotoxicity.
- Proteomics and metabolomics analysis did not show significant cellular alteration.

GRAPHICAL ABSTRACT

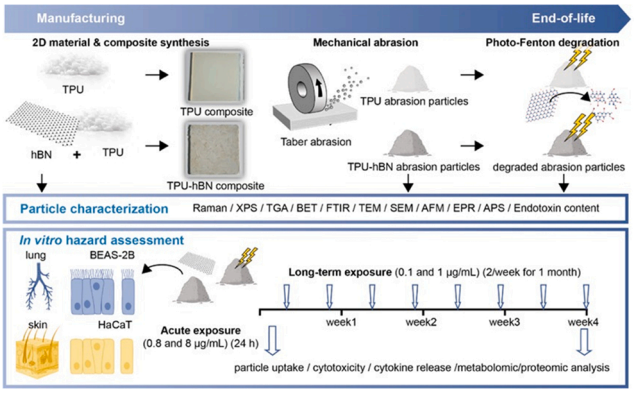

* Corresponding authors.
E-mail addresses: a.bianco@ibmc-cnrs.unistra.fr (A. Bianco), bengt.fadeel@ki.se (B. Fadeel), mpelin@units.it (M. Pelin).

https://doi.org/10.1016/j.jhazmat.2024.134686
Received 25 March 2024; Received in revised form 14 May 2024; Accepted 20 May 2024
Available online 22 May 2024

ARTICLE INFO

Keywords:
2D materials
Cytotoxicity
Composites
Omics
Life cycle perspective

ABSTRACT

Hexagonal boron nitride (hBN) is an emerging two-dimensional material attracting considerable attention in the industrial sector given its innovative physicochemical properties. Potential risks are associated mainly with occupational exposure where inhalation and skin contact are the most relevant exposure routes for workers. Here we aimed at characterizing the effects induced by composites of thermoplastic polyurethane (TPU) and hBN, using immortalized HaCaT skin keratinocytes and BEAS-2B bronchial epithelial cells. The composite was abraded using a Taber® rotary abraser and abraded TPU and TPU-hBN were also subjected to photo-Fenton-mediated degradation mimicking potential weathering across the product life cycle. Cells were exposed to the materials for 24 h (acute exposure) or twice per week for 4 weeks (chronic exposure) and evaluated with respect to material internalization, cytotoxicity, and proinflammatory cytokine secretion. Additionally, comprehensive mass spectrometry-based proteomics and metabolomics (secretomics) analyses were performed. Overall, despite evidence of cellular uptake of the material, no significant cellular and/or protein expression profiles alterations were observed after acute or chronic exposure of HaCaT or BEAS-2B cells, identifying only few pro-inflammatory proteins. Similar results were obtained for the degraded materials. These results support the determination of hazard profiles associated with cutaneous and pulmonary hBN-reinforced polymer composites exposure.

1. Introduction

2D materials display many properties such as atomically thin morphology, broad surface area, and layered structure that make them attractive for several applications [1-3]. Beyond graphene (the first atomically thin crystal), a large variety of 2D materials has been explored, including hBN, a layered material, isostructural to graphene, which is sometimes referred to as "white graphene" [4]. Each hBN layer is thus composed by a hexagonal sp^2-bonded network with strong in-plane polar bonds between nitrogen and boron atoms, resulting in a large energy band-gap (5–6 eV), instead of different layers that are held together by van der Waals forces [5]. Due to its remarkable physicochemical properties, such as chemical inertness, stability to oxidation, lubricity, high mechanical flexibility, intrinsic anisotropy, piezoelectricity, excellent thermal conductivity, and electrical insulation [5–8], hBN has attracted considerable interest in applications ranging from electronics and photonics to catalysis [9]. In particular, hBN and related composites have emerged as industrial-relevant materials, which can address many challenges in complex microelectronics systems such as the need to develop thermal conductive polymers to meet the demand of heat management of advanced electronic devices [10]. Due to the large band-gap, low dielectric constant, and excellent in-plane thermal conductivity, hBN can be considered an ideal thermal conductive and electrically insulative filler for polymer-based materials [11]. Notably, TPU is widely used as a versatile elastomer with high flexibility, tear resistance, chemical inertness, ductility and processability [12]. TPU properties can be enhanced in terms of thermal conductivity and electrical insulation by adding hBN as a filler [10,13-17].

The potential use of these novel hBN-based composites thus necessitates the assessment of the toxicological profile of these materials to ensure human safety upon occupational and/or consumer exposure. Skin contact and inhalation can be considered the most relevant exposure routes for these materials. To date, while several in vitro and in vivo studies investigated the effects of boron nitride nanotubes (BNNTs) [18, 19], the number of studies on hBN and relevant composites are still limited. Recent work using primary human monocyte-derived dendritic cells has shown that hBN has negligible effects on cells up to 50 μg/mL [20], while other investigators found no or modest effects of hBN using PMA-differentiated THP-1 cells (a model of macrophages) [21]. Regarding models of cutaneous exposure, hBN caused slight cytotoxic effects in human normal skin fibroblasts, albeit at high concentrations (>100 μg/mL) [22,23]. The authors also found that hBN improved the wound healing process at non-toxic concentrations by increasing cell proliferation and migration and by lowering reactive oxygen species production [23]. Using the human HaCaT keratinocyte cell line, hBN as well as other related composites, such as polyhydroxyalkanoate/chitosan hBN-incorporated composites, and polyaniline/hBN nanocomposites, were shown to display negligible effects on cell viability [24,25]. Concerning in vitro models of inhalation (pulmonary) exposure, BN nanoparticles (at concentrations <100 μg/mL) exerted a slight toxic potential but did not lead to death of human primary alveolar epithelial cells [26]. Domanico et al. [27] demonstrated that hBN nanosheets were cytotoxic only at a high concentration (200 μg/mL) in primary murine tracheal epithelial cells and at moderate concentrations in the human lung adenocarcinoma cell line A549. Another study investigated the effects of hBN nanosheets with different geometries, and found that only hBN with sharp edges induced a dose-dependent cytotoxicity in the human lung adenocarcinoma cell line H460 [28]. It is noted, however, that these experiments were conducted at high concentrations of hBN (80 μg/mL).

Previous work has addressed the potential toxicity of composites reinforced with graphene-based materials (GBMs) [29,30]. However, safety issues posed by particles released from hBN-reinforced composites during the potential weathering and degradation across the material life cycle, have not been explored. Nevertheless, one may assume that hBN particles incorporated in different matrices can be released and their physicochemical properties (lateral dimension, thickness, surface defects) can be transformed during the life-time of a product. Importantly, the toxicological impact may differ for such released materials when compared to the pristine counterpart. The present study focused on the toxicological effects of an hBN-reinforced composite of TPU and hBN versus the individual components, TPU and hBN, following weathering (abrasion). Additionally, the materials were subjected to photo-Fenton degradation to assess the potential impact of the degradation products. Cytotoxic effects were evaluated in vitro considering the two exposure routes of greatest relevance in an occupational setting, namely skin contact and inhalation [31,32]. To this aim, we used the human immortalized non-malignant HaCaT keratinocyte (skin) cell line and BEAS-2B bronchial epithelial (lung) cell line. Cells were exposed for 24 h (acute exposure) or twice per week for 4 weeks (long-term exposure) and the effects were evaluated in terms of cellular uptake, cytotoxicity, and cytokine release. Additionally, mass spectrometry-based proteomics and metabolomics studies were also conducted. Overall, the present study is the first attempt at exploring the hazard profile associated with cutaneous and inhalation exposure to hBN-reinforced composites.

2. Materials and methods

2.1. hBN and hBN-reinforced TPU composites

TPU (ELASTOLAN 1185 A) was purchased from BASF, Germany and used without further modifications. Few-layer hBN flakes used as fillers were produced by BeDimensional SpA. In particular, bulk hBN was

exfoliated in *N-methyl-2-pirrolidone* (NMP) as described in patent No. WO2017089987A1, and by Castillo et al. [33]. During the exfoliation process, the shear forces and the cavitation generated by the turbulent flow of the solvent passing through the nozzle, promote the exfoliation of the bulk hBN into single and few layers of hBN. The as-produced dispersion was reprocessed, using nozzles with different diameters of 0.2, 0.15 and 0.1 mm. The as-prepared hBN dispersion in NMP was dried using a rotary evaporator (Heidolph Heivap Industrial, FKV Srl, Italy) at a bath temperature of 80 °C. While the pressure decreased down to 5 mbar, 6 L of dimethyl sulfoxide was added (Merck KGaA, Germany). To obtain the hBN powder, the mixture was freeze-dried. The TPU and TPU-hBN composite was prepared by melt mixing using the twin screw extruder followed by the hot-press machine. The melt-mixing was carried out using a twin-screw extruder (45 L/D, Bandera, Italy) at 190 °C and 250 rpm. TPU and TPU loaded with hBN pellets (2 wt%) were vacuum-dried at 90 °C for 3 h. The TPU film samples (10 ×10 cm^2) were prepared by hot pressing of pristine and TPU-hBN pellets. Hot pressing was carried out at 190 °C under 2.5 T of pressure for 15 min.

2.2. Mechanical abrasion and particle collection

Exfoliated hBN powder and composite films of neat TPU and TPU-hBN (2%) (both ~80 cm^2) were prepared as described above. To study the toxicity of the particles released during use and end-of-life phases of the composite materials, TPU and TPU-hBN were abraded using a Taber® abrader as described previously [29] with a few modifications. Briefly, we used a Taber® Rotary Platform Abrasion Tester (Model 1700, Taber, North Tonawanda, NY) equipped with an S-42 sandpaper strip wrapped around a rubber wheel and an additional weight of 0.5 kg. The particles released from the abrasion were suctioned from the abrasion area by a small probe that was placed next to the abrasive wheel above the film, with a reduced suction area that helped to increase the vacuum suction power near the sample surface. The abraded particles were collected on Nuclepore track-etched polycarbonate membranes (Whatman, UK) of 0.2 μm pore size. The flow rate was generated by the Fisherbrand® Diaphragm pump (Fisher Scientific AG, 4153 Reinach, Switzerland) and monitored in the range of 7 to 10 L/min using a mass flow controller (Model GFC37, Aalborg, NY).

2.3. Physicochemical characterization of materials

2.3.1. Transmission electron microscopy (TEM)

The samples were prepared by drop casting the hBN dispersion in NMP onto an ultrathin C-film on holey carbon 400 mesh Cu grids, from Ted Pella Inc. The hBN dispersions were diluted 1:20. The grids are stored under vacuum at room temperature to remove the solvent residues. TEM images are taken in a JEOL JEM-1011 transmission electron microscope, operated at an acceleration voltage of 100 kV.

2.3.2. Atomic force microscopy (AFM)

The exfoliated hBN dispersions were diluted 1:30 in fresh NMP, and 100 mL of the diluted dispersions were drop-cast onto Si/SiO_2 wafers and dried at 50 °C overnight. AFM images were acquired with a Bruker Innovas AFM in tapping mode using silicon probes (frequency = 300 kHz, spring constant = 40 N/m). The statistical analysis of the flakes thickness was performed by measuring more than 100 flakes from the AFM images. Statistical analyses were fitted with log-normal distributions and performed with the WSxM Beta 4.0 software.

2.3.3. Size distribution of abraded particles

An aerodynamic particle sizer (APS; Model 3321, TSI Incorporated, Minnesota, USA) which measures particles in the range from 0.5 μm to 20 μm, was used to determine the particle size distribution. The data represent mean values ± S.D. of 9 or 10 measurements for TPU and TPU-hBN samples, respectively. The Origin 2018 software (OriginLab Corporation, Northampton, MA) was used to fit the particle size distributions to a log-normal distribution. The collection of abraded particles was performed without APS to reduce possible particle loss.

2.3.4. Scanning electron microscopy (SEM)

The morphology of abraded particles was characterized using a Nova NanoSEM 230 (FEI, Japan) with an acceleration voltage of 10 kV. The powders were deposited on conductive carbon tape and a thin layer of platinum (10 nm) was sputter-coated on top of the samples.

2.3.5. Raman spectroscopy

Raman spectra were acquired using an InVia Renishaw microspectrometer, with a 532 nm laser source boasting a power density of 1 $mW/\mu m^2$. The comprehensive examination involved multiple readings taken at 30–40 randomly selected locations on each material.

2.3.6. Thermogravimetric analysis (TGA)

Thermogravimetric analyses were conducted utilizing a TGA Q50 instrument from TA Instruments in a controlled air atmosphere. The temperature ramp was systematically set at 10 °C per min, spanning the range from 100 °C to 900 °C.

2.3.7. X-ray Diffraction (XRD)

XRD data were recorded using a Philips (Panalytical) XPert MPD diffractometer equipped with Cu KAlpha1 (0.154056 nm) at 40 kV and 40 mA. Diffraction patterns were systematically collected over a range of 5–60° 2θ at a scan rate of 0.01° $2\theta min^{-1}$ and a scan velocity of 0.004° s^{-1}.

2.3.8. Scanning electron microscopy (SEM), scanning transmission electron microscopy (STEM) and energy-dispersive X-ray spectroscopy (EDX)

SEM and STEM images, elemental mapping, and EDX analysis was conducted on hBN, TPU and TPU-hBN samples using a GeminiSEM 500 field emission instrument (Zeiss). STEM images were acquired on lacey copper grids. SEM, EDX, and elemental mapping were performed using powdered material.

2.4. Photo-Fenton-based material degradation

The photo-Fenton reaction was performed as reported in our previous study on hBN,[34] by employing a UV lamp (Blak-Ray B100AP, USA). The UV lamp operates with 100 W power to produce continuous UV light at 365 nm with a ballasted bulb. The dispersion of hBN, abraded TPU and abraded TPU-hBN composites (0.62 mL of 0.78 mg/mL), 20 μL of 1 mM $FeCl_3 \bullet 6\ H_2O$ and 4.92 mL of H_2O were mixed in a quartz vial. The pH of the resulting mixture was adjusted to 4 with 0.1 M HCl. The quartz vial was capped with a septum and 200 μL of 50 mM H_2O_2 was added every 10 h. The quartz tube was kept 6 cm away from the UV lamp under stirring. The total reaction was carried out for 100 h. Additional 20 μL of 1 mM $FeCl_3 \bullet 6\ H_2O$ were added every ~35 h. Sonication of the suspension for 3 min was carried out in an ultra-sonication bath every 10 h approximately to refresh the suspension. Aliquots of 100 μL were collected at 0, 20, 50 and 100 h for TEM and Raman analyses as described below, and at 100 h for biological experiments.

2.5. Characterization of degraded materials

2.5.1. TEM analysis

For TEM characterization of degraded materials, 10 μL of each suspension of degraded hBN, TPU, and TPU-hBN samples were deposited on carbon coated copper grids and dried for 24 h before the analysis. The samples were analyzed using a Hitachi H7500 microscope (Tokyo, Japan) with an accelerating voltage of 80 kV, equipped with a AMT Hamamatsu camera (Tokyo, Japan).

2.5.2. Raman spectroscopy

Raman spectra for hBN were recorded at room temperature using a Renishaw Raman Microscope InVia Reflex equipped with a 2D-CCD

camera. All samples were prepared by putting the solution of investigated material on Si/SiO_2 substrate with Au electrode to quench the fluorescence from TPU and left to evaporate the solvent. The samples were focused with a 100 × objective and were excited with a laser (λ = 785 nm). The samples were irradiated with a laser power of 1%. At least 3 accumulations lasting 10 s each were recorded, and 5 points were averaged.

2.6. Toxicological assessment using in vitro models

2.6.1. Material dispersion

Stock dispersions of the tested materials (hBN, TPU and TPU-hBN, and their corresponding degraded products) were prepared at the concentration of 0.5 mg/mL in 0.1% bovine serum albumin (BSA) (Sigma-Aldrich) by ultrasonic bath sonication. Stock dispersions were then diluted to final freshly prepared working concentrations (0.8 and 8 μg/mL for acute exposure; 0.1 and 1 μg/mL for repeated chronic exposure) in complete culture medium (see below) and used immediately for analyses.

2.6.2. Endotoxin content

The endotoxin content of each material was determined using the Pierce™ Chromogenic Endotoxin Quant Kit (ThermoFisher Scientific). The assay was conducted in accordance with the manufacturer's guidelines. The samples were measured at 405 nm using a Tecan Infinite F200 plate reader (Tecan, Sweden). The concentration of endotoxin in each material was calculated based on the standard curve generated using lipopolysaccharide (LPS) (0, 0.1, 0.25, 0.5, 1.0 EU/mL).

2.6.3. Human cell lines

2.6.3.1. HaCaT cell line. The human immortalized skin keratinocyte cell line HaCaT was purchased from Cell Line Services at Deutsches Krebsforschungszentrum (DKFZ) (Eppelheim, Germany) and cultured in high glucose Dulbecco's Modified Eagle's Medium (DMEM), supplemented with 10% FBS, 2 mM L-glutamine, 100 U/mL penicillin and 100 mg/mL streptomycin. Cells were maintained in a humidified atmosphere at 37 °C and 5% CO_2 and sub-cultured twice a week upon reaching confluence.

2.6.3.2. BEAS-2B cell line. The human immortalized human bronchial epithelial cell line, BEAS-2B (European Collection of Cell Cultures), was cultured in serum-free bronchial epithelial cell growth medium (BEGM) (Lonza) supplemented with BulletKit™ (Lonza). The latter supplement included recombinant epidermal growth factor (EGF), bovine pituitary extract, GA-1000 (gentamicin sulfate and amphotericin-B), hydrocortisone, insulin, retinoic acid, transferrin, triiodothyronine, and epinephrine. Before seeding, flasks and plates were coated with a mixture of 0.01 mg/mL fibronectin, 0.03 mg/mL bovine collagen type I, and 0.01 mg/mL BSA for 2 h. Cells were cultured in a humidified atmosphere at 37 °C with 5% CO_2 and subcultured when the cells reached 80% confluence.

2.6.4. Cytotoxicity assessment

Cytotoxic effects in HaCaT and BEAS-2B cell lines were evaluated using the LDH release assay (CytoTox® Non-Radioactive Cytotoxicity Assay) (Promega), following the manufacturer's instructions. Treatment of cells for 30 min with lysis solution (provided in the kit) represented the positive control. After exposure, 50 μL aliquots of culture medium were collected for LDH measurements and transferred into a clear 96-well plate in triplicate and mixed with an equal volume of CytoTox® 96 Reagent. After a 30 min incubation at room temperature in the dark, 50 μL of stop solution was added and optical density (OD) of each sample was measured at 490 nm using the FLUOstar® Omega microplate reader (BMG LABTECH) or the Tecan Infinite F200 microplate reader (Tecan, Sweden). LDH release is reported as % of the positive control (total cell lysis).

2.6.5. Cytokine secretion

For HaCaT cells, cytokine release was quantified after 24 h exposure or 4 weeks of repeated exposure for each material. LPS (10 μg/mL; Sigma-Aldrich) and untreated cells were used as positive and negative controls, respectively. Samples were centrifugated for 10 min at 5.000 rpm to spin down residual cells. Supernatants were stored at − 70℃ until cytokine analysis. The release of human interleukin (IL)− 8 and tumor necrosis factor (TNF)-α was measured by enzyme-linked immunosorbent assay (ELISA; human IL-8 and TNF-α ELISA Kit; Diaclone, Besançon, France). Samples were analysed using the FLUOstar® Omega microplate reader (BMG LABTECH; Ortenberg, Germany). For BEAS-2B cells, cytokine release was assessed in culture media after 24 h exposure to each material. LPS (0.1 μg/mL; Sigma-Aldrich) and untreated cells were used as positive and negative controls, respectively. Samples were collected as detailed above. IL-8 and TNF-α release was determined using human IL-8 and TNF alpha ELISA kits (Invitrogen, Sweden). Samples were analysed using a Tecan Infinite F200 plate reader. Data were expressed as pg/mL and the results are the mean values ± S.E.M. of three independent experiments performed in duplicate.

2.6.6. Cellular uptake

HaCaT and BEAS-2B cells were seeded in complete growth medium one day before treatment. Cells were then exposed for 24 h to the indicated materials at a concentration of 20 μg/mL. Subsequently, control and exposed cells were detached by trypsinization, centrifuged, and resuspended in the fixation solution (2.5% glutaraldehyde in 0.1 M phosphate buffer). Fixed cells were stored at + 4℃. Samples were then immersed in a 1% solution of osmium tetroxide in 0.1 sodium phosphate buffer for 1 h at 4 °C. The samples subsequently underwent dehydration using a gradient of ethanol, followed by acetone, and were subjected to LX-112 infiltration before being embedded in LX-112 resin (Ladd Research Industries, Vermont, OH). Ultrathin sections (50–80 nm) were prepared using a Leica EM UC6 microtome and were further contrasted with uranyl acetate and lead citrate. The samples were examined using a Hitachi HT 7700 electron microscope. Image acquisition was carried out using the 2kx2k Veleta CCD camera manufactured (Olympus).

2.7. Multi-omics analysis of exposed cell lines

2.7.1. Sample preparation for omics analysis

HaCaT and BEAS-2B cells were seeded in 150 cm^2 polystyrene tissue culture flasks. For the acute exposure study, cells were maintained until reaching 70% confluency before being left unexposed or exposed to hBN, abraded TPU or TPU-hBN, at a concentration of 8 μg/mL for 24 h. Cells were then trypsinized and washed in ice cold PBS before being centrifugated. Cell pellets (4×10^6 cells/pellet, 3 biological replicates, each prepared in 4 technical replicates) and their corresponding conditioned media (2 mL) were then collected and kept at − 70℃ until analysis. For the chronic/long-term exposure study, cell pellets and conditioned media were collected after 4 weeks exposure at a concentration of 1 μg/mL. The harvesting of samples (in 5 technical replicates for each biological replicate) was identical to the procedure described for the acute cytotoxicity study. Chemicals used for sample preparation were purchased from Merck Spa (Milano, Italy) and solvents from Carlo Erba (Milano, Italy). Proteomics grade trypsin was purchased by Sigma-Aldrich (St. Louis, MO, USA). Tandem mass tag (TMT) 16-plex Isobaric Mass Tagging Kit and Reagents were purchased from Thermo Fisher Scientific (Rockford, IL, USA).

2.7.2. Proteomics and metabolomics

A bottom-up proteomics approach was applied for the analysis of the cell protein content using high-resolution mass spectrometry. Cells first underwent a lipid extraction process then the protein pellet was

reduced, alkylated at Cys residues and digested with trypsin. The resulting peptides were again suspended in buffer solution and were labeled using isobaric Tandem Mass Tags (TMTpro™ 16plex Label Reagent Set; Thermo Fisher Scientific), following the manufacturer's protocol and analyzed. For the metabolomics analysis of cell culture supernatant, we applied a conservative sample preparation: an aliquot of cell culture medium was filtered using molecular sieves with 10 K MWCO. The flow–through was collected, evaporated under nitrogen then re-suspended and analyzed as described below.

2.7.3. Proteomics and TMT labeling

Samples of both cell lines were treated with 2-propanol for the extraction of the lipid content in 1 mL per 1 million cells ratio. The supernatant was collected, evaporated and samples were stored at − 20 °C. The resulting protein pellet was dried and re-suspended in 100 mM triethylammonium bicarbonate (TEAB) at pH 8. A bicinchoninic acid (BCA) assay was performed with Pierce™ BCA Protein Assay Kits (Thermo Fisher Scientific) to assess the total protein content. An aliquot containing 50 μg protein/sample, was then diluted to a final volume of 100 μL of 100 mM TEAB. 10 μL of 100 mM Dithiothreitol reducing solution was added and samples were incubated at 56 °C shaking at 600 rpm for 30 min, then 30 μL of 100 mM iodoacetamide alkylating solution was added and incubated at room temperature for 20 min. Proteins were then precipitated in acetone overnight. The digestion was performed using trypsin from porcine pancreas in a ratio 1:50 to protein amount. At this point, peptides were ready for the labeling step: as indicated by the vendor, the ratio between peptide to label and TMT reagent (dissolved in acetonitrile) was 1:10. The reaction was incubated at RT and 400 rpm for 1 h. With the specific format, 6 × 0.5 mg (per tag) of TMTpro™ 16plex Label Reagent, the scheme followed for the labeling step is reported below (see Table S1). To terminate the labeling reaction, 5 μL of 5% hydroxylamine. All 16 channels were combined in a single sample that was cleaned-up and fractionated using Oasis C18 spin columns (Thermo Scientific™ Pierce™ C18 Spin Columns). Columns were activated using ACN and 3% ACN was used for the conditioning. A linear gradient to 50% ACN was used for the elution/fractionation of the peptides, resulting in 8 separate fractions that were grouped as follows: 1 + 5, 2 + 6, 3 + 7, 4 + 8. Samples were dried and re-suspended in 3% ACN for the injection on the LC-MS system.

2.7.4. Data acquisition and analysis

Labeled tryptic peptides were separated using an UltiMate 3000 UHPLC system (Dionex) and analyzed by an Orbitrap Explorix 480 mass spectrometer equipped with a Nanospray Flex™ Ion Source (Thermo Fisher Scientific). Chromatographic run started with a loading and desalting step on a trap column, after that the peptides were eluted from an Aurora C_{18} nanocolumn (75 mm × 250 mm, 1.6 μm particle size) (Ion Opticks, Fitzroy, Australia). A gradient started from 3% B (B = 80:20 ACN/H_2O + 0.1% formic acid; A = H_2O + 0.1% formic acid) then to 5% after 20 min, 10% after 40 min, 25% after 80 min, 55% after 1 h 50 min and 15 min at 95%, followed by column cleaning and reconditioning. The flow rate was set to 300 nL/min. Total run time was 2 h and 30 min. For each sample 500 ng of peptides were loaded on the column. Peptides were analyzed in positive ESI mode, with a capillary voltage set to 2.0 kV. The RF lens was set to 40% and the AGC target was set to 200%. Data acquisition was performed in Data Dependent Acquisition with a scan range set from 350 to 1200 *m/z* at 120,000 resolution, followed by MS/MS acquisition of 60 *m/z* transmission windows, each having a fixed 10 Da width. MS/MS spectra were acquired by setting a Higher-energy Collisional Dissociation (HCD) mode. All acquired RAW data were analyzed using Proteome Discoverer 2.5 software (Thermo Fisher Scientific). MS/MS spectra were searched against a *Homo sapiens* FASTA file downloaded from UNIPROT (20211030) with 20316 reviewed sequences reported. The following modifications were selected: cysteine carbamidomethylation and TMTpro as fixed, methionine oxidation and phosphorylation at serine, threonine and tyrosine as variable. The intensities of the reporter ions were used to derive the relative abundance of the corresponding proteins. In accordance with the preliminary BCA assay, we assumed that an equal amount of protein lysate was analyzed in each run. Data was thus first normalized by the total peptide amount observed in each analytical run and then re-normalized across all runs within each acute and chronic, HaCaT or BEAS-2B experiment. Only protein hits at a maximum 1% false discovery rate against a decoy database and positively assigned based on at least two unique peptide hits were retained for quantification. For Differential Expression (DE) analysis a p-value threshold of 0.05 was considered. The ratio to highlight a relevant change in protein expression was arbitrarily set to + /− 10% with respect to control. The DE plots were generated in MATLAB R2020b [35]. The number of DE proteins as well as the number of common proteins between the different experimental conditions are shown using an upset plot generated with the upSetR R package [36]. In proteins that were DE between the treatment conditions and the untreated ones, the over-representation of specific KEGG [37] and Reactome [38] signaling pathways was assessed. To find statistically significant instances, a Fisher's exact test is implemented considering as background all proteins measured in the respective experimental conditions. The resulting p-values were FDR corrected using the BH method [39] and pathways identified as being enriched with an FDR below 10% were considered significant. To avoid redundancy, only significant pathways that did not overlap more than 85% with respect to the ones corresponding to lower FDR values were further considered and are reported in Supplementary File 1. The pathway analysis was conducted in R v4.2.3 (R [40]) using the clusterProfiler R package (T. [41]). The KEA3 [42] algorithm was applied through the online web-service, using as input the upregulated phosphoproteins or proteins highlighted by the TMT proteomics analysis. To build protein-protein interaction networks we obtained high-confidence human interactors from the publicly available STRING [43], BioGRID [44] and IntACT [45] databases and applied them to our lists of upregulated DE proteins for each experimental condition considering as well proteins that just had an abundance ratio difference above 10%. For STRING, database version 11.5 containing the complete interactions data considering all sources was used and filtered to include only entries with a combined score above 0.7. For BioGRID, version 4.4.218 data file in the mitab format that contained a dataset of interactors with physical interactions supported by independent validations was used. The latter file was filtered to exclude entries without an associated confidence value. For the IntACT database, the psimitab from 13/07/2022 was used and filtered to keep only interactions with a confidence score above 0.7. Interaction pairs obtained from the different databases were overlapped and merged in a joint dataset. Network modules with more closely connected entries [46] were extracted from the analyzed network using MONET software [47]. For this, the Modularity optimization method with undirected edges was applied, and the desired average nodes degree in the identified modules was set to 10. The modules were sorted based on the number of nodes they included. Next, Reactome and KEGG pathways over-represented in individual modules were assessed. Background datasets for individual phenotypes were composed of all proteins that were used to construct the full-scale network of the respective condition. The procedure for identifying over-represented signaling pathways associated with each module was applied in the same manner as for the full list of DE proteins. For data handling and visualization, additional R packages were used: RColorBrewer [48], readr [49], stringr [50], gtools [51], gridBase [52], tidygraph [53], biomaRt [54] and readxl [55].

2.7.5. Polar metabolomics study

An untargeted metabolomics study, mostly focusing on polar (low LogP) compounds, was carried out on supernatant collected from cell culture. The cell supernatant (500 μL aliquots) was not extracted with organic solvents (that would extract more apolar species like lipids) but simply filtered using molecular sieves with 10 K MWCO and the flow–through was collected and evaporated under N_2 flux. Samples were re-

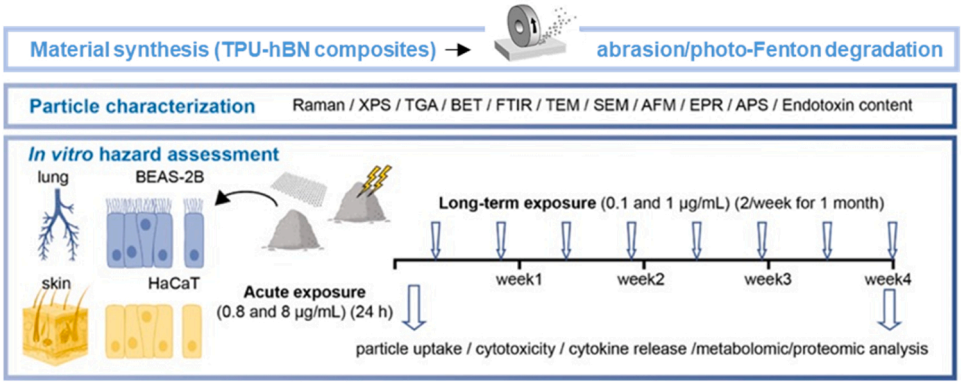

Fig. 1. Study design. hBN and hBN-reinforced TPU composite (TPU-hBN) were prepared and subjected to abrasion and degradation, followed by an exhaustive physicochemical characterization. Two human immortalized (non-malignant) cell models were used in order to assess the potential effects following acute or long-term (chronic) exposures in vitro.

suspended in 100 µL 3% ACN + 0.1% formic acid, 10 µM Glipizide was used as internal standard, for retention time realignment, peak picking and data normalization.Samples were analyzed using an Acquity UPLC system (Waters) coupled to a TripleTOF 5600 + (AB Sciex Instruments) equipped with a DuoSpray Ion Source. The solvents used for the chromatographic run were A = H_2O + 0.1% formic acid and B = ACN + 0.1% formic acid to elute samples on a reverse phase HSS T3 column (2.1 ×100 mm, 1,8 µm), setting the temperature at 45 °C. A linear gradient started from 3% B to reach 80% in 6 min and keeping it for 2 min, with 3 min of cleaning and reconditioning thereafter. The flow rate was set at 0.45 mL/min. The mass spectrometer performed a survey scan from 100 to 1000 *m/z* with a Sequential Window Acquisition of All Theoretical Mass Spectra (SWATH) acquisition [56], setting an acquisition window of 60 *m/z* over the scan range. The source temperature was set at 450 °C and the curtain gas was set at 50 L/h. For MS/MS acquisition part, the collision energy (CE) was set at 20 V and the Declustering Potential (DP) at 80 V. The acquired RAW data were analyzed using MSDial software tool (version 4.9) [57]. SWATH data were searched against the embedded ion library of 16,481 unique compounds. Main search parameters were: mass tolerance 0.05 Da, minimum peak height 500 ions/second, retention time tolerance: 0.1 min. All peak areas were normalized by the internal standard. Only features having accurate mass AND fragment ion matches were assigned to a metabolite hit. Unsupervised data analysis, consisting of Principal Component Analysis and heatmap analysis was carried out using Metaboanalyst software [58]. Following normalization by the area of the internal standard, the data for all the features positively annotated was log transformed, mean-centered and divided by the standard deviation of each variable. Heatmap analysis was performed using the top 25 most altered features (identified from an ANOVA analysis).

2.8. Statistical analysis

Results are presented as mean values ± S.E.M. of at least 3 independent experiments. The analysis was performed by one- or two-way ANOVA followed by Bonferroni's multiple comparison post-test, using

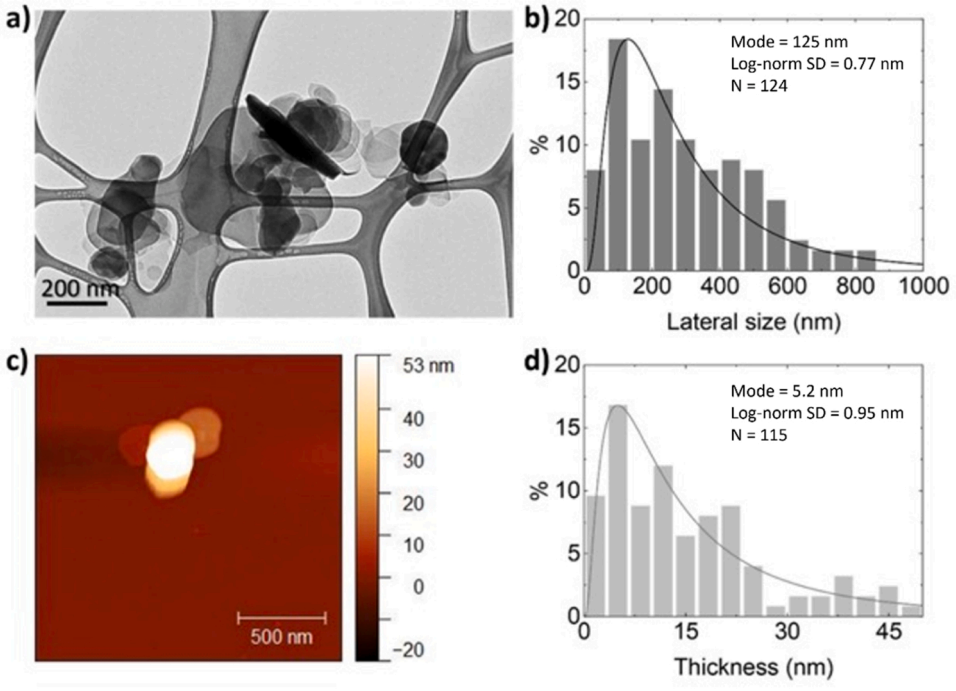

Fig. 2. TEM and AFM analysis of the exfoliated hBN flakes. (a) Representative TEM image of hBN flakes, and (b) the associated size distribution. (c) Representative AFM image of hBN flakes, and (d) the associated log-normal fitted histogram.

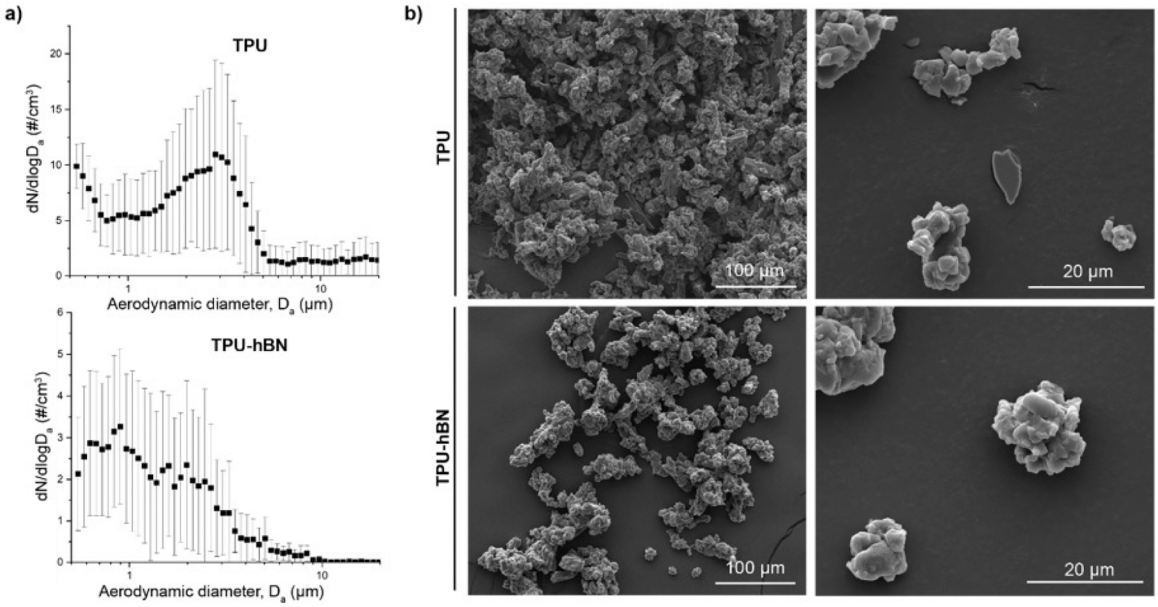

Fig. 3. Characterization of abraded particles from TPU and TPU-hBN composite: (a) Particle size distributions on the semi-log scale of the abraded particles, measured by APS. The results show mean ± S.E.M. from 9 (TPU) and 10 (TPU-hBN) independent measurements; (b) SEM images of abraded particles from TPU and TPU-hBN composite.

GraphPad Prism. Results were considered statistically significant for $p < 0.05$.

3. Results and discussion

3.1. Experimental design

The overview of the presented study design is schematically represented in Fig. 1. hBN was used to produce an industrially relevant hBN-reinforced TPU composite (TPU-hBN; 2 wt% hBN). The neat TPU and TPU-hBN were abraded using a standardized protocol to simulate a mechanical abrasion process, as previously reported for a graphene-reinforced polymer [29]. To further achieve a life cycle perspective, hBN and particles of abraded TPU, and TPU-hBN were also submitted to a photo-Fenton-based degradation process. A comprehensive physicochemical characterization of all the materials was conducted using an extensive panel of different methods (Raman, XPS, TGA, BET, FTIR, TEM, SEM, AFM, EPR, APS, endotoxin content) to help in the interpretation of in vitro data. The in vitro hazard assessment of both the abraded and degraded materials was performed using epidermal keratinocytes (i.e. HaCaT) and bronchial epithelial cells (i.e. BEAS-2B), two commonly used models of the skin and lungs, respectively. These cell lines are immortalized but non-malignant, thus representing a useful model of normal skin and lungs, respectively. The cells were submitted to an acute exposure (24 h) (0.8, 8 µg/mL) or a repeated long-term exposure regimen (twice per week for 4 weeks) (0.1, 1 µg/mL) and evaluated with respect to material uptake, cytotoxicity, and cytokine secretion. Finally, proteomics and metabolomics (secretomics) analyses were conducted on exposed cells and cell supernatants, respectively. The doses applied in the acute exposure setting are equal to the cumulative doses applied in the long-term exposure. These concentrations, which are low in comparison to most nanotoxicological studies, are based on our previous long-term in vitro studies on graphene oxide (GO) [59]. The aim here was to improve the translational power of the model (i.e., low-dose, long-term).

3.2. Physicochemical characterization

The as-produced hBN flakes were characterized by TEM and AFM imaging (Fig. 2). The lateral size of hBN flakes was determined by measuring their diameter and evaluated through the associated histogram. The data then was fitted with a log-normal distribution model, as it properly describes the particle sizes in fragmented systems [60]. The distribution mode is reported as it constitutes the most stable measured value, while the homogeneity of the sample is captured by the log-normal standard deviation. For the exfoliated hBN (see Methods), TEM analysis indicated a lateral size mode of 125 nm (Fig. 2b), and AFM indicated a thickness mode of 5.2 nm (Fig. 2d).

The materials used for the in vitro study described below (hBN and abraded TPU and TPU-hBN) underwent a comprehensive characterization employing a number of techniques to evaluate their physicochemical characteristics. In Fig. S1a-c, STEM images of the distinct materials — hBN, TPU, and TPU-hBN, respectively — are presented, showcasing structures within the 200 nm scale. For hBN, circular flakes with a distribution size of 63.3 ± 24.7 nm are observed (Fig. S1d), while TPU exhibits particles with a size distribution of 34.9 ± 9.4 nm (Fig. S1e). Fig. S1f displays TGA results in an air atmosphere. Residual weight loss, attributed to oxygen functional groups in nanomaterial flakes, was 1.8% for h-BN, 94.8% for TPU, and 89.7% for TPU-hBN. Notably, a substantial mass loss between 100–300 °C is associated with the decomposition of the TPU polymer. The higher residual weight loss (5.1%) in TPU-hBN compared to TPU indicates the effect of hBN addition. Fig. S1g presents XRD results, revealing an amorphous band in TPU and TPU-hBN, due to their lack of crystallinity. In hBN, a single peak at 23.83° (indexed as hBN, JCPDS 34–0421) signifies the single-phase hBN (002) plane, also present in TPU-hBN. Fig. S1h shows the Raman spectra of the different materials. For TPU and TPU-hBN, similar bands are evident, including a band with maxima at 2928 cm^{-1} and 2866 cm^{-1} , attributed to asymmetric and symmetric C-H stretching vibrations of CH_2 groups. [61] Additionally, C═O stretching vibrations of ester and urethane groups manifest at 1737 cm^{-1} and 1700 cm^{-1} [62,63]. The intense band between 1615 cm^{-1} and 1539 cm^{-1} corresponds to -C═C- stretching vibrations of the aromatic ring [62,63]. The Raman band at 1539 cm^{-1} is attributed to N-H deformation and C-N stretching vibrations (amid II band) [61]. Significantly, at approximately 1205 cm^{-1} , discernible are the coupled vibrations of C-N and C-O within the urethane group (urethane amid IV band) [61]. At 1126 cm^{-1} , the Raman band is likely ascribed to the in-plane deformation vibrations of aromatic =C-H [61].

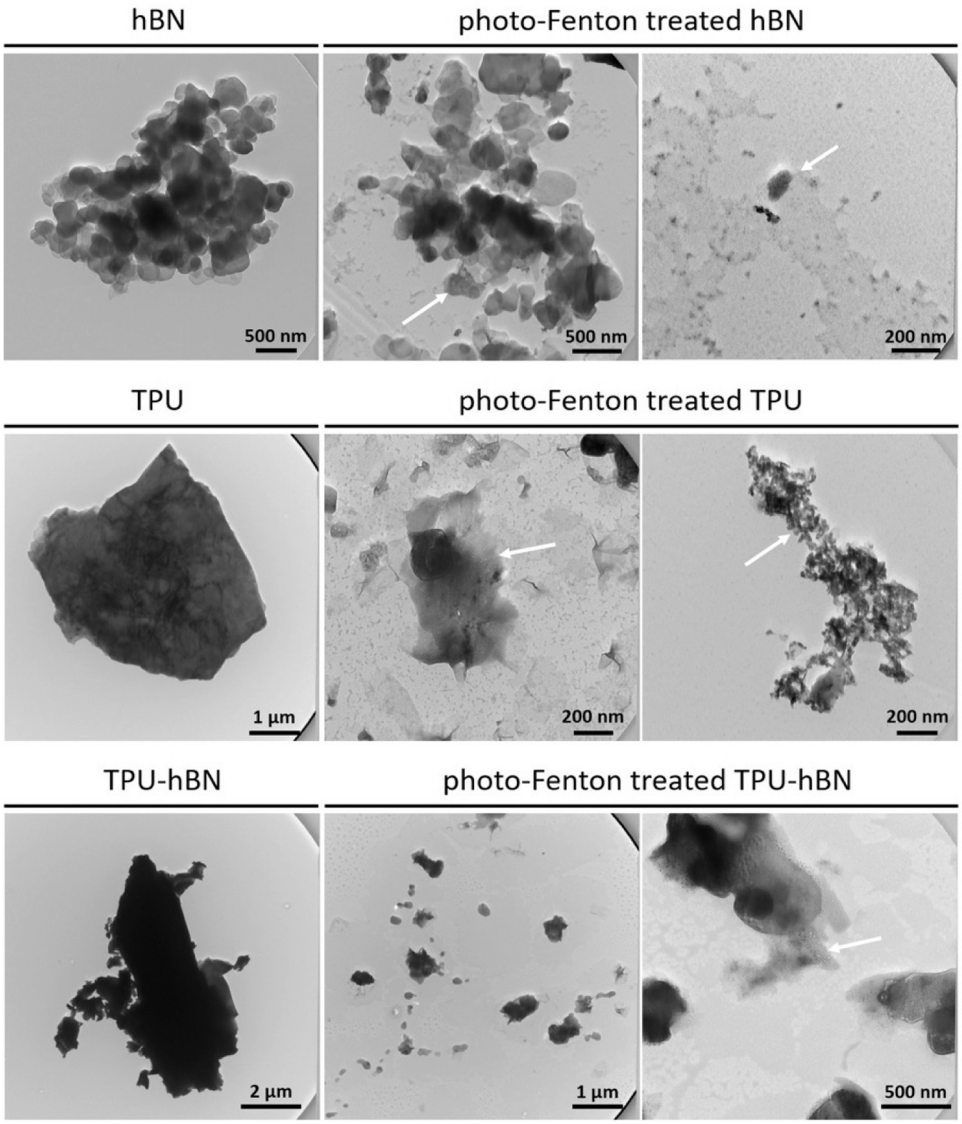

Fig. 4. TEM images of non-degraded and photo-Fenton treated hBN, abraded TPU and TPU-hBN composite. The white arrows show the degradation of the materials. The edges of hBN were crumpled, and holes and fragments were found on TPU or TPU-hBN after 100 h (see also Fig. S3).

On the other hand, in the hBN sample, the characteristic E_{2g} peak is observed at 1370 cm^{-1} using an excitation laser at 532 nm [64]. This same peak is visible in TPU-hBN while it is absent in the initial TPU material, confirming the presence of hBN. The materials were also characterized by SEM, elemental mapping, and EDX analyses. Data shown in Fig. S2a-c correspond to hBN. A uniform sample with a consistent content of B and N is evident in the image mapping (Fig. S2a), while the EDX spectra reveal the elemental composition with 51.0 wt% of boron, 48.2 wt% of nitrogen, and 0.8 wt% of oxygen. In Fig. S2d-f, the characterization of TPU is depicted. The SEM image shows the presence of charges, attributed to the insulating nature of the sample, and a similar phenomenon was observed in the TPU-hBN sample. In a SEM, bright spots on a material can be attributed to various interactions between the electron beam and the atoms within the sample. Specifically, these bright spots are often due to backscattered electrons or secondary electrons generated during these interactions [65]. The mapping image reveals the presence of oxygen and carbon, with carbon as the predominant element. The corresponding EDX spectra elucidated the elemental composition, showing 80.7 wt% of carbon and 19.3 wt% of oxygen. The distribution of hBN within the TPU-hBN composite was investigated using SEM, elemental mapping, and EDX (Figs. S2g-i). Carbon and oxygen identified are the predominant elements. Additionally, the EDX analysis indicates a slight increase in the percentage of nitrogen, approximately 1.5 wt%, while carbon constituted 77.8 wt% and oxygen 20.7 wt%. These findings are consistent with observations derived from other characterization techniques such as Raman and TGA, demonstrating the presence of hBN in the TPU-hBN composite.

To understand if the abraded particles were found in the fraction that can deposit in the alveolar region of the lung (below 4 µm) [66], we determined the aerodynamic size of the released particles online during the abrasion process of TPU and TPU-hBN by APS measurements (Fig. 3). Abraded particles from neat TPU exhibited a mean aerodynamic diameter of approx. 2.8 µm, whereas most particles released from TPU-hBN exhibited aerodynamic sizes of around 0.8 - 2 µm (Fig. 3a). Moreover, the number of particles measured by APS was much smaller for TPU-hBN abrasion and it took a much longer abrasion time to collect similar number of particles as for TPU abrased particles. SEM imaging confirmed a broad size distribution of the abraded particles with different shapes and sizes (Fig. 3b). Although the particles appear to be larger in the SEM images as compared to their aerodynamic diameter, this observation could be explained by the fact that SEM images consider the projected area, whereas the aerodynamic diameter depends on the

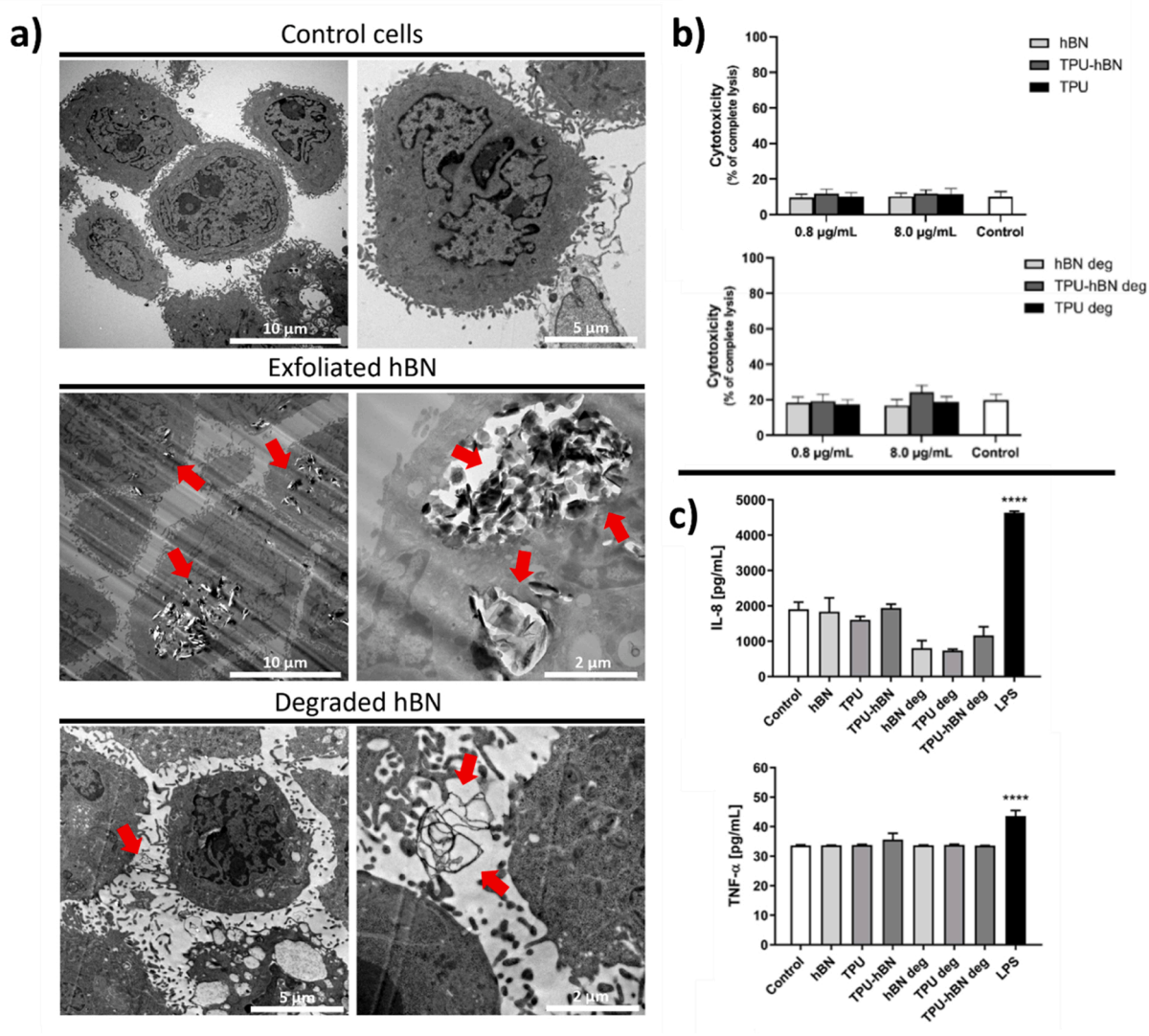

Fig. 5. Acute effects induced in HaCaT cells by hBN, TPU, TPU-hBN and their degraded products (0.8 and 8.0 µg/mL) after 24 h exposure. (a) TEM analysis of HaCaT cells after acute exposure to exfoliated and degraded hBN for 24 h at 20 µg/mL concentration. Red arrows represent particles inside or around the cells. (b) Cytotoxic effects evaluated by LDH release assay; results are expressed as % of cytotoxicity with respect to the positive control (complete lysis; 100% of LDH release). Statistical analysis vs negative control: two-way ANOVA and Bonferroni's post-test. (c) Release of IL-8 and TNF-α from HaCaT cells exposed to hBN, TPU, TPU-hBN, and their degraded products, for 24 h (8 µg/mL). Inflammatory mediators were quantified in HaCaT cells media by specific ELISA assays. As a positive control, HaCaT cells were exposed to 10 µg/mL LPS. Statistical differences vs negative control: * ** *, $p < 0.0001$ (One-way ANOVA and Bonferroni post-test). Data are the mean ± S.E. M. of three independent experiments performed in triplicate.

shape, density and orientation of the particles with respect to its direction of motion [67].

3.3. Photo-Fenton degradation

The abraded TPU and TPU-hBN composite, and the control hBN material, were then subjected to the UV-assisted photo-Fenton reaction. This reaction is known to generate highly potent hydroxyl radicals. The efficacy of the photo-Fenton reaction has been well-documented in the literature for the degradation of diverse materials [68-71]. Initial insights on the degradation of hBN, TPU, and TPU-hBN were obtained through TEM analyses at the end of the 100 h treatment (Fig. 4 and Fig. S3). Remarkably, after the treatment, a portion of hBN sheets underwent a transformation into highly porous fragments, completely losing their characteristic 2D sheet-like layered structure. The analysis of the same sample also exhibited zones of partial degradation, with pronounced crumpling at the edges and a considerable number of surface holes. Regarding abraded TPU and TPU-hBN, significant alterations were observed compared to the initial materials. The distinct edge structure vanished, presenting a substantial amount of fragmented and holy structures on both TPU and TPU-hBN after 100 h. The efficacy of the photo-Fenton reaction with respect to the degradation of nanomaterials has been well-documented in the literature [68-71]. Our previous studies showed near-complete degradation of hBN sheets after 100 h, which contrasts somewhat with the present findings. These differences might be due to variations in the dispersibility and size of the hBN [69].

The UV-light degraded fragments derived from the abraded materials and the control hBN were also characterized by Raman spectroscopy. Fig. S4 displays the comparison of hBN, TPU as well as TPU-hBN Raman spectra before and after the treatment under the photo-Fenton conditions for 100 h. Before irradiation, all peaks in the TPU-hBN spectrum could be assigned to either hBN or TPU. The in-plane vibration $E_{2\,g}$ peak of hBN is positioned at ~1378 cm^{-1} using the 785-nm excitation laser [34,72], while the rest signals are contributed by TPU [61]. Before irradiation, in TPU, the band at 3065 cm^{-1} can be attributed

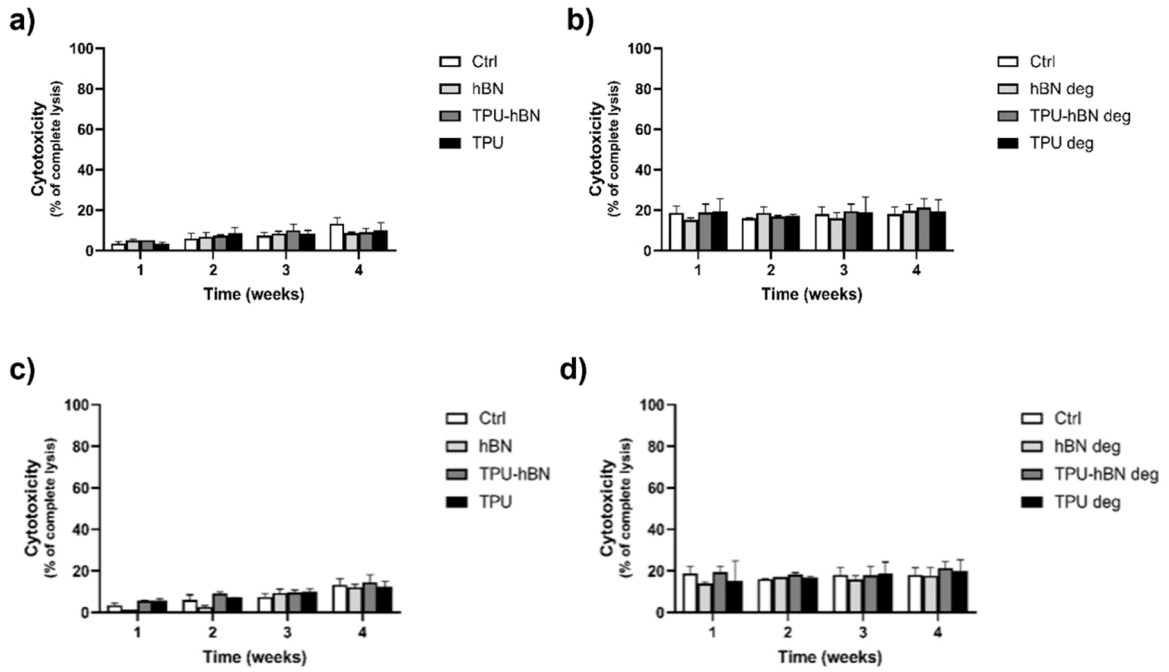

Fig. 6. Effects of hBN, TPU, TPU-hBN and their degraded products at 0.1 μg/mL (a,b) and at 1.0 μg/mL (c,d) on HaCaT cells over four weeks of repeated exposures, assessed through the LDH release assay. Results are expressed as % of cytotoxicity with respect to the positive control (complete lysis; 100% of LDH release) and are the mean ± S.E.M. of three independent experiments performed in triplicate. Statistical analysis vs negative control: two-way ANOVA and Bonferroni's post-test.

to =C-H stretching vibrations of the aromatic rings (Fig. S4a). The peaks at 2928 cm^{-1} and 2875 cm^{-1} are assigned to the asymmetric and symmetric C-H stretching vibrations of CH_2 groups of the polymer, respectively. The two small, close peaks located at 1730 cm^{-1} and 1702 cm^{-1}, are attributed to C═O stretching vibrations of the ester and urethane groups, respectively. The most intense peak at 1617 cm^{-1} represents -C═C- stretching vibrations of aromatic rings. The band at 1539 cm^{-1} can be ascribed to N-H deformation and C-N stretching vibrations (amid II band), while the peak at 1439 cm^{-1} comes from C-H deformation vibrations of CH_2 groups. The last two peaks, at 1251 cm^{-1} and 1185 cm^{-1} can be assigned to C-N and C-O vibrations of urethane groups (urethane amid IV band), and aromatic =C-H in-plane deformation vibrations, respectively [61]. The same peaks in the spectrum of TPU are also present in the spectrum of TPU-hBN, where the additional peak at ~1378 cm^{-1} derives is from hBN. After irradiation for 100 h, similarly to what shown by TEM images, Raman analysis allowed to identify areas in the deposited samples significantly different from the starting material (Fig. S4a and S4b). Many peaks between 3200 cm^{-1} and 1500 cm^{-1} disappeared. The remaining peaks are broadened, likely due to the transformed/degraded polymer. The position of the peak from hBN in TPU-hBN is shifted to ~1365 cm^{-1} and slightly less intense when compared to the starting TPU-hBN. We also observed that this peak in hBN (Fig. S4c) after treatment is wider compared to initial hBN, with the maximum of the peak remaining at the same position. However, similarly to the TEM results, the Raman analysis also demonstrated that there is a certain amount of TPU that is not completely degraded (Fig. S5).

3.4. Endotoxin assessment

For the biological studies, the test materials have to be screened for possible endotoxin contamination. To this end, the endotoxin content was quantified using the Limulus Amebocyte Lysate (LAL) assay. No significant interference from the materials with the assay was observed. According to the LPS standard curve, the endotoxin concentrations of hBN, TPU and TPU-hBN were all below the FDA-mandated 0.5 EU/mL limit (Fig. S6).

3.5. Effects on skin keratinocytes

3.5.1. Acute effects after 24 h of exposure

We then evaluated the effects of hBN, abraded particles of TPU and TPU-hBN, and relevant degradation products, on HaCaT cells following 24 h exposure with respect to cellular uptake (TEM), cell viability (LDH release), and cytokine secretion (Fig. 5). TEM analysis showed that exfoliated (pristine) hBN particles (20 μg/mL) were taken up by keratinocytes after an acute exposure of 24 h (Fig. 5a). However, degraded hBN particles were not internalized or were not visible in the cells. Similarly, no cellular uptake was observed for the other materials tested (at 24 h; Fig. S7), probably because of their bigger dimensions. To the best of our knowledge, no data are currently available concerning the internalization of pristine hBN and/or hBN composites in keratinocytes as shown by microscopy analysis, despite evidence of hBN cellular uptake provided previously based on flow cytometry analysis of other skin cell types, such as human dermal fibroblasts [23]. However, a comparison can be made in this regard to other 2D materials, such as graphene and its derivatives. Indeed, TEM analysis of HaCaT keratinocytes exposed for 24 h to GO and few-layer graphene, at similar concentrations to those used in present study for hBN (10 - 100 μg/mL), demonstrated that both materials were internalized by the cells [73,74]. This observation was also supported by confocal microscopy analysis in reflection mode carried out on the same cellular model [75]. Intriguingly, it was demonstrated that even after recovery conditions (24 h exposure, followed by an additional 48 h culture in fresh medium without the materials), few-layer graphene was still retained into the phagosomes of keratinocytes [74]. On the whole, these data, together with the evidence of the present study revealing the presence of hBN inside HaCaT cells, thus demonstrate that 2D materials can be internalized even in non-phagocytic cells such as skin cells. This phenomenon was further corroborated by in vivo models (mice topically treated with GBMs) [76] and in 3D in vitro models of the human epidermis (SkinEthic™ reconstructed human epidermis) [77], showing small depots of GBMs within the epidermis.

The cytotoxicity was measured by the assessment of LDH release. hBN, TPU and TPU-hBN, as well as their degradation products, elicited

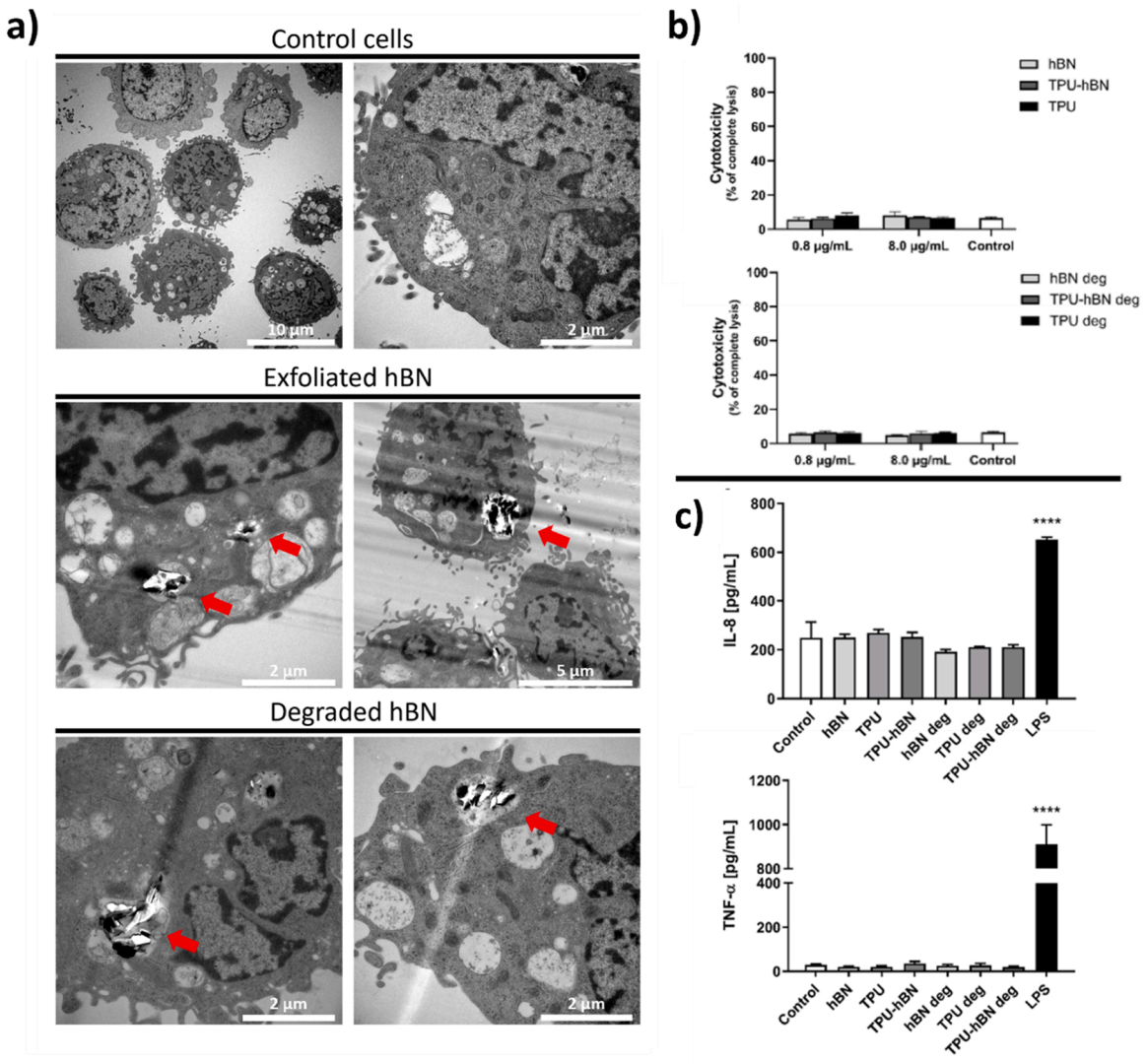

Fig. 7. Acute effects induced in BEAS-2B cells by hBN, TPU, TPU-hBN and their degraded products (0.8 and 8.0 µg/mL) after 24 h exposure. (a) TEM analysis of BEAS-2B cells after acute exposure to exfoliated and degraded hBN for 24 h at 20 µg/mL concentration. Red arrows represent particles inside the cells. (b) Cytotoxic effects evaluated by LDH release assay; results are expressed as % of cytotoxicity with respect to the positive control (complete lysis; 100% of LDH release). Statistical analysis vs negative control: two-way ANOVA and Bonferroni's post-test. (c) Release of IL-8 and TNF-α from BEAS-2B cells exposed to hBN, TPU, TPU-hBN and their degraded products, for 24 h (8 µg/mL). Inflammatory mediators were quantified in BEAS-2B cells media by specific ELISA assays. As a positive control, BEAS-2B cells were exposed to 0.1 µg/mL LPS. Statistical differences vs negative control: * ** *, $p < 0.0001$ (One-way ANOVA and Bonferroni post-test). Data are the mean ± S.E. M. of three independent experiments performed in triplicate.

negligible plasma membrane damage, comparable to that measured for the negative control (Fig. 5b). Moreover, exfoliated hBN at concentrations up to 100 µg/mL did not influence LDH release (Fig. S8a), suggesting excellent biocompatibility of hBN. This observation is in line with the limited literature data on skin cells currently available. In particular, in dermal fibroblasts hBN did not exert any cytotoxicity up to the concentration of 100 µg/mL after 24 h exposure, with a significant effect observed only at higher concentrations (i.e. 400 µg/mL) [22]. Similarly, a subsequent study showed a reactive oxygen species (ROS)-dependent reduction of cell viability in human dermal fibroblasts only at hBN concentrations > 150 µg/mL [23]. Also in keratinocytes, a weak cytotoxic effect was observed. In HaCaT cells, only a slight reduction of cell viability (around 6%) was observed for hBN up to the concentration of 83.3 µg/mL after 24 h exposure. Intriguingly, a similar result was noticed for a set of hBN composites with polyaniline at different ratios [24]. However, the cytotoxic potential of hBN, as evidenced also for other 2D materials, could rely on the material dimension. Indeed, a more potent effect seems to be exerted by 2D structures constituted by hBN quantum dots (dimension: 10–15 nm), reducing cell viability after 24 h already at the concentration of 5 µg/mL [78].

To evaluate if the tested materials were able to trigger an inflammatory response in HaCaT cells after 24 h exposure (8.0 µg/mL), the cellular release of IL-8 and TNF-α was evaluated (Fig. 5c). No significant alterations in the levels of IL-8 and TNF-α were observed for the materials tested, while LPS (10 µg/mL) triggered a significant increase in IL-8 and TNF-α release as expected. Currently, no evidence about a possible inflammogenic potential of hBN and/or related composites in keratinocytes has been previously reported. However, the lack of IL-8 and TNF-α induction contrasts with previous studies on GBMs which triggered cytokine secretion in HaCaT cells even at low concentrations in absence of cell viability loss [73]. Thus, hBN seems less inflammogenic than GBMs.

3.5.2. *Long-term effects after repeated exposures for 1 month*

To evaluate the possible long-term effects induced by hBN, TPU, TPU-hBN and their degraded products, HaCaT cells were repeatedly

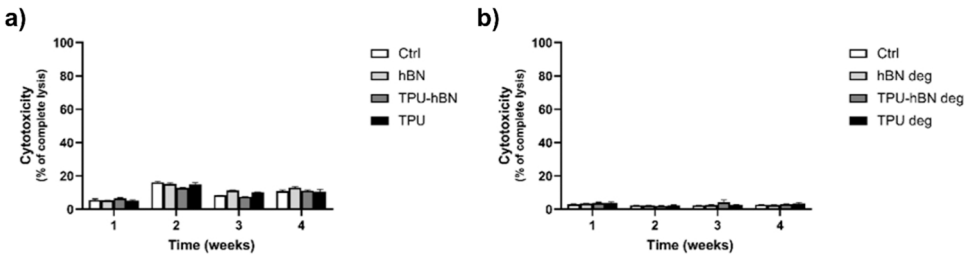

Fig. 8. Effects of exfoliated hBN, abraded TPU and TPU-hBN (a), and their degraded products (b) (1.0 μg/mL) on plasma membrane integrity in BEAS-2B cells over four weeks of repeated exposures, assessed through the LDH release assay. Results are expressed as % of cytotoxicity in terms of LDH release with respect to the positive control (complete lysis; 100% of LDH release) and are the mean ± S.E.M. of three independent experiments performed in triplicate. Statistical analysis vs negative control: Two-way ANOVA and Bonferroni's post-test.

exposed over four weeks to each material twice a week at a concentration of 0.1 μg/mL (Figs. 6a,b) and 1.0 μg/mL (Fig. 6c,d). Cell viability was evaluated by means of LDH release. No significant loss of cell viability was observed for any of the tested materials, highlighting an excellent biocompatibility even after 1 month of repeated exposure. This result is in line with a previous study on GBMs which did not alter cell viability after 30 days of repeated exposures at the concentration of 5 μg/mL despite alterations in the cell metabolome were found [79]. Furthermore, no TNF-α secretion was observed at 4 weeks of exposure (Fig. S9). However, the cells remained responsive to LPS after 4 weeks of cell culture (Fig. S9).

3.6. Effects on bronchial (lung) cells

3.6.1. Acute effects after 24 of exposure

We then evaluated the acute effects of hBN, abraded particles of TPU and TPU-hBN, and relevant degradation products (0.8 and 8 μg/mL), on BEAS-2B bronchial epithelial cells after 24 h exposure with respect to cellular uptake (TEM), cell viability (LDH release), and cytokine secretion (Fig. 7). TEM analysis showed that the exfoliated hBN particles were internalized by BEAS-2B cells after 24 h (Fig. 7a). Evidence of cellular uptake of the degraded hBN particles (Fig. 7a) as well as the other materials tested were found (Fig. S11). The potential cytotoxicity of hBN and abraded particles of TPU and TPU-hBN (0.8 and 8 μg/mL), as well as their degradation products, was also evaluated, and the results indicated no significant cytotoxicity in the human bronchial epithelial cell line BEAS-2B (Fig. 7b). Moreover, no significant cytotoxic effects were observed for exfoliated hBN at high concentrations (up to 100 μg/mL) (Fig. S8b), again testifying to the excellent biocompatibility of hBN. We also evaluated if the tested materials were able to trigger an inflammatory response after 24 h exposure (8.0 μg/mL). However, neither abraded or degraded hBN materials (hBN, TPU, TPU-hBN) triggered any secretion of IL-8 and TNF-α (Fig. 7c) while LPS (0.1 μg/mL) triggered cytokine release as expected. The present findings accord with a previous study using primary human dendritic cells in which hBN did not trigger cytokine secretion even at concentrations up to 50 μg/mL [20], suggesting that hBN is fairly innocuous.

3.6.2. Long-term effects after repeated exposures for 1 month

BEAS-2B cells were also exposed to the same set of materials at a concentration of 1 μg/mL over a period of 4 weeks and monitored with respect to LDH release each week. The results showed no cytotoxicity (Fig. 8a,b). Taken together, hBN, TPU, TPU-hBN and their degraded products were found to be non-cytotoxic towards BEAS-2B cells following both acute and long-term exposure regimens.

3.7. Multi-omics analysis (acute and long-term exposures)

3.7.1. Proteomics analysis of keratinocytes and bronchial cells

Proteomics analysis was performed on samples collected from both HaCaT and BEAS-2B cells acutely exposed for 24 h (8.0 μg/mL) or repeatedly exposed twice a week for 4 weeks (1.0 μg/mL) (Fig. 9), quantifying several thousands of proteins per each individual analytical run. Through the TMT labeling strategy, we derived the relative abundance of each given protein in all four experimental conditions (control, hBN, TPU and TPU-hBN). Given that the above-reported cytotoxicity data demonstrated that degraded materials did not alter cells parameters in comparison to the non-degraded ones, omics analysis were performed only on the latters. The data acquired for the two cell lines, for acute and chronic exposure conditions, are reported in Supplementary File 1. This

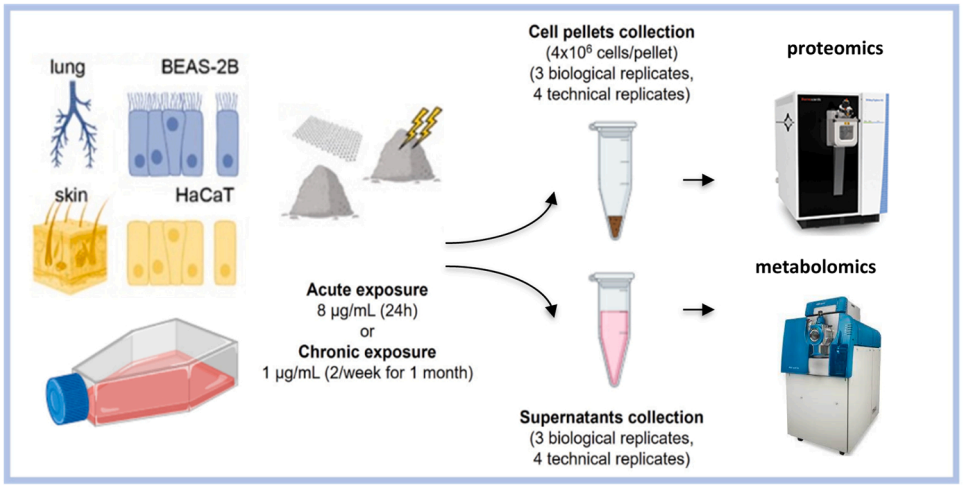

Fig. 9. Study design for the proteomics and metabolomics analyses. BEAS-2B or HaCaT cells were exposed acutely (24 h) or repeatedly twice a week for 4 weeks, and samples were collected for mass spectrometry-based proteomics and metabolomics analyses.

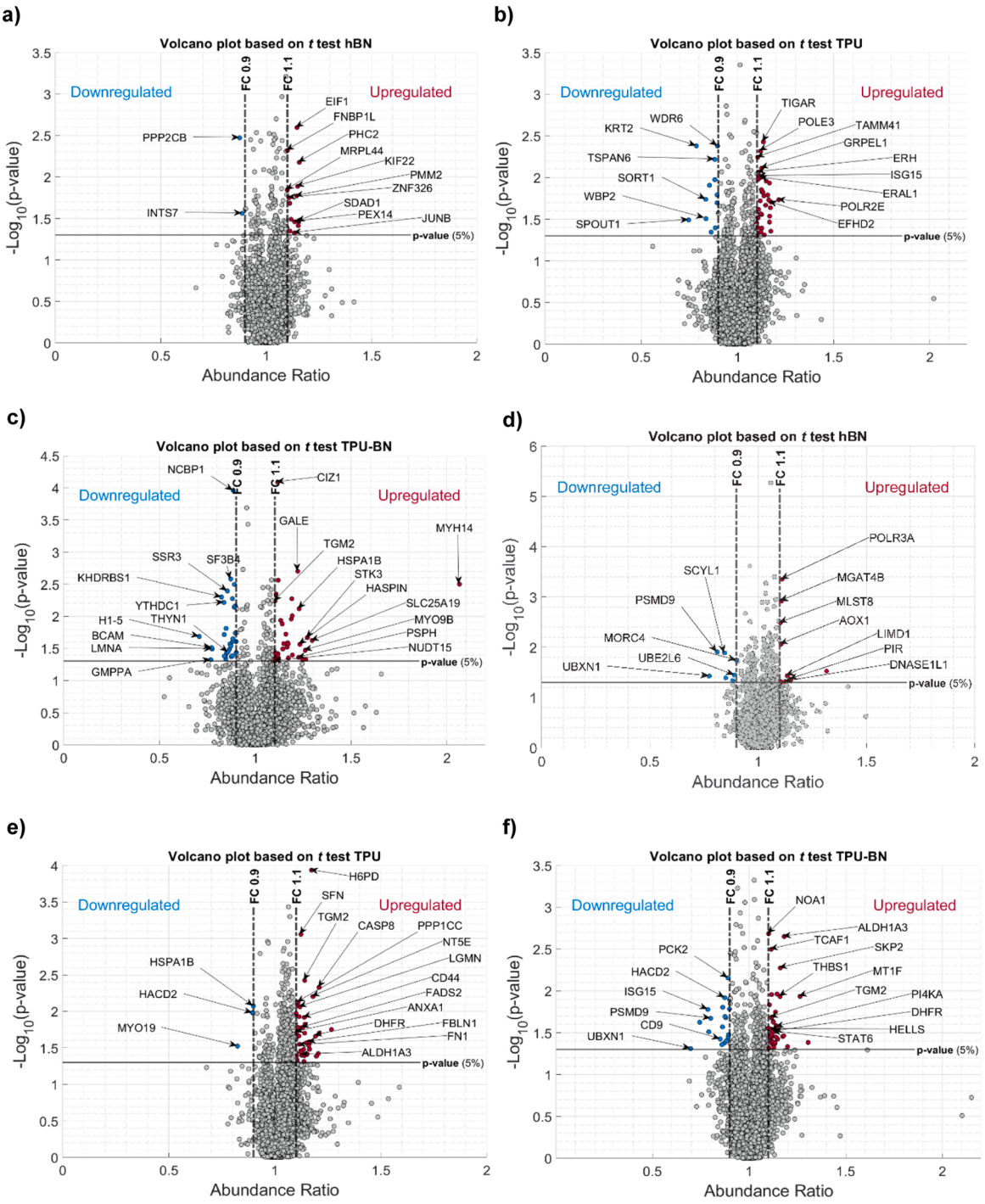

Fig. 10. Differential expression analysis for acutely exposed BEAS-2B (a-c) and HaCaT (g-i) cells and chronically (repeatedly) exposed BEAS-2B (d-f) and HaCaT (j-l) cells. The proteins that are common between the studied groups or highly expressed or known to be pro-inflammatory are shown.

excel file reports, in separated sheets, all the raw data from both cell lines and both exposure conditions, expressed as over/under expression ratio of the three materials (hBN, TPU and TPU-hBN) versus control. Subsequent statistical analysis did not reveal major patterns of up- or down-regulation following exposure to the tested materials. Hence, differential expression (DE) analysis applied to the treatment conditions compared to the control ($p < 0.05$; abundance ratio change </> 10%), highlighted a very small number of up- and downregulated proteins with minor overlaps between the different conditions (Fig. S11). hBN- and TPU-treated cells provided a maximum of 24 and 47 DE proteins for the acute exposure of the HaCaT and BEAS-2B cells, respectively, while the TPU-hBN composite induced between 37 and 77 DE proteins for HaCaT and BEAS-2B cells, respectively. We constructed volcano plots (depicting fold-change versus significance on the x- and y-axes, respectively) to visualize the proteomics data (Fig. 10). Several proteins with known inflammatory activity were identified including PDCD4 and IKBIP for HaCaT cells acutely exposed to TPU-hBN, and THBS1 and STA6 for BEAS-2B cells chronically exposed to TPU-hBN (Fig. 10a-l). However, the DE proteins could not be assigned with confidence to any specific biological pathway, suggesting that changes were minimal and

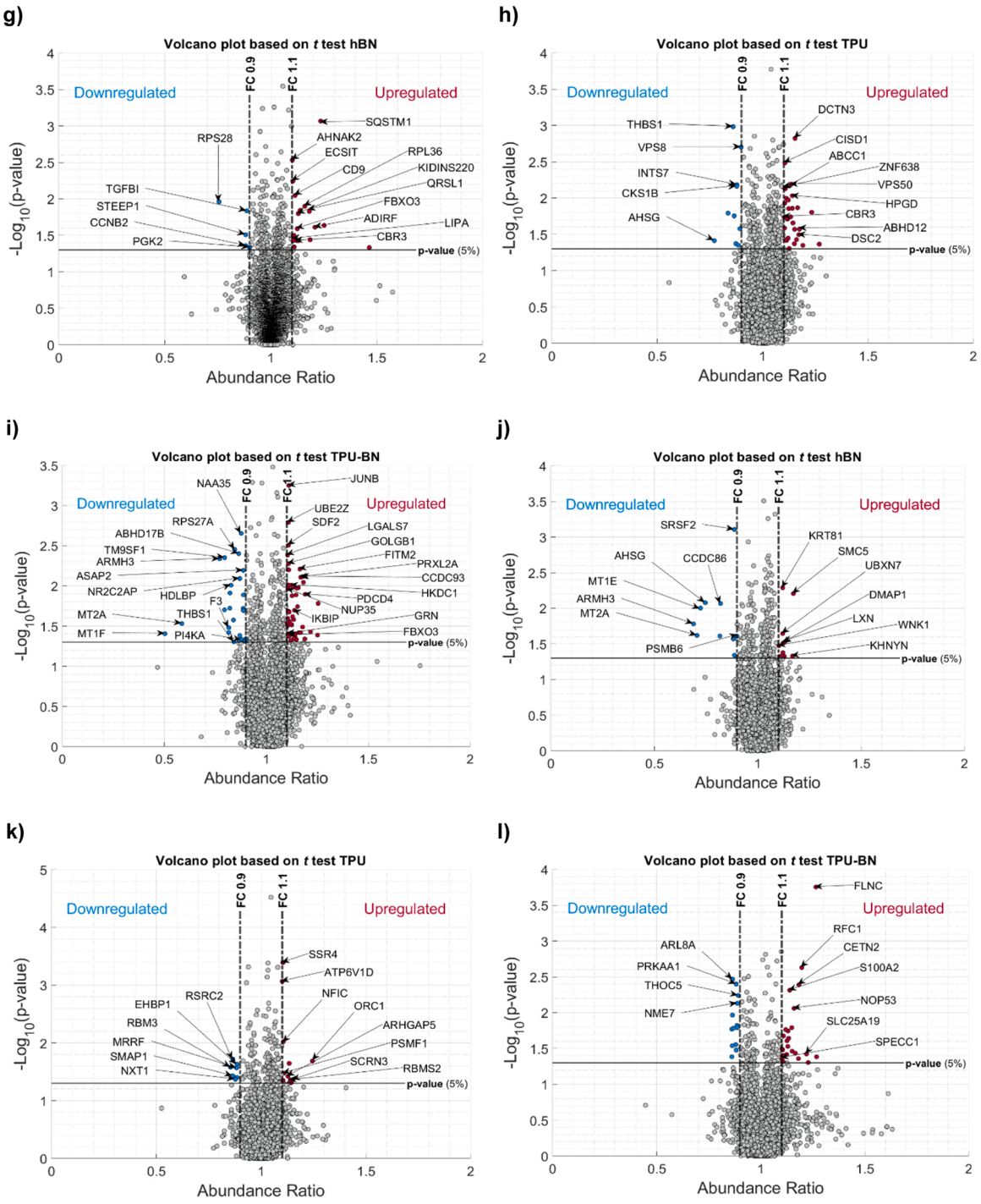

Fig. 10. (*continued*).

inconsistent.

Furthermore, to provide context for the identified DE proteins, we constructed protein-protein interaction (PPI) networks between the DE proteins and all the proteins that were found to have an abundance ratio change above 10% for the specific experimental conditions. This allowed us to interpret the identified DE proteins in a much broader context that is specific to the studied experimental conditions with the main aim of investigating possible associations of these proteins with molecular pathways that could raise safety concerns. To construct these networks, only high-confidence interactions from STRING, BioGRid and IntACT databases were used (see Methods). To extract the closest network neighborhood that could highlight the biological functions of the identified DE proteins, MONET network decomposition tool [47], which is able to split a PPI network into modules with specific biological functions, was applied to the data using the modularity optimization method (M1). Fig. S12 shows the signaling pathways associated with the decomposed network modules that contained at least one DE protein. Enrichment of proteasome-related pathways for BEAS-2B cells treated with TPU and TPU-hBN was observed when considering acute exposure, while enrichment of endocytosis-related pathways was noted in the case of chronic exposure of BEAS-2B cells to TPU-hBN. For HaCaT cells, DE proteins associated with endoplasmic reticulum-related pathways were enriched after acute exposure to TPU-hBN. Importantly, no enrichment in pro-inflammatory pathways was observed in BEAS-2B cells or HaCaT

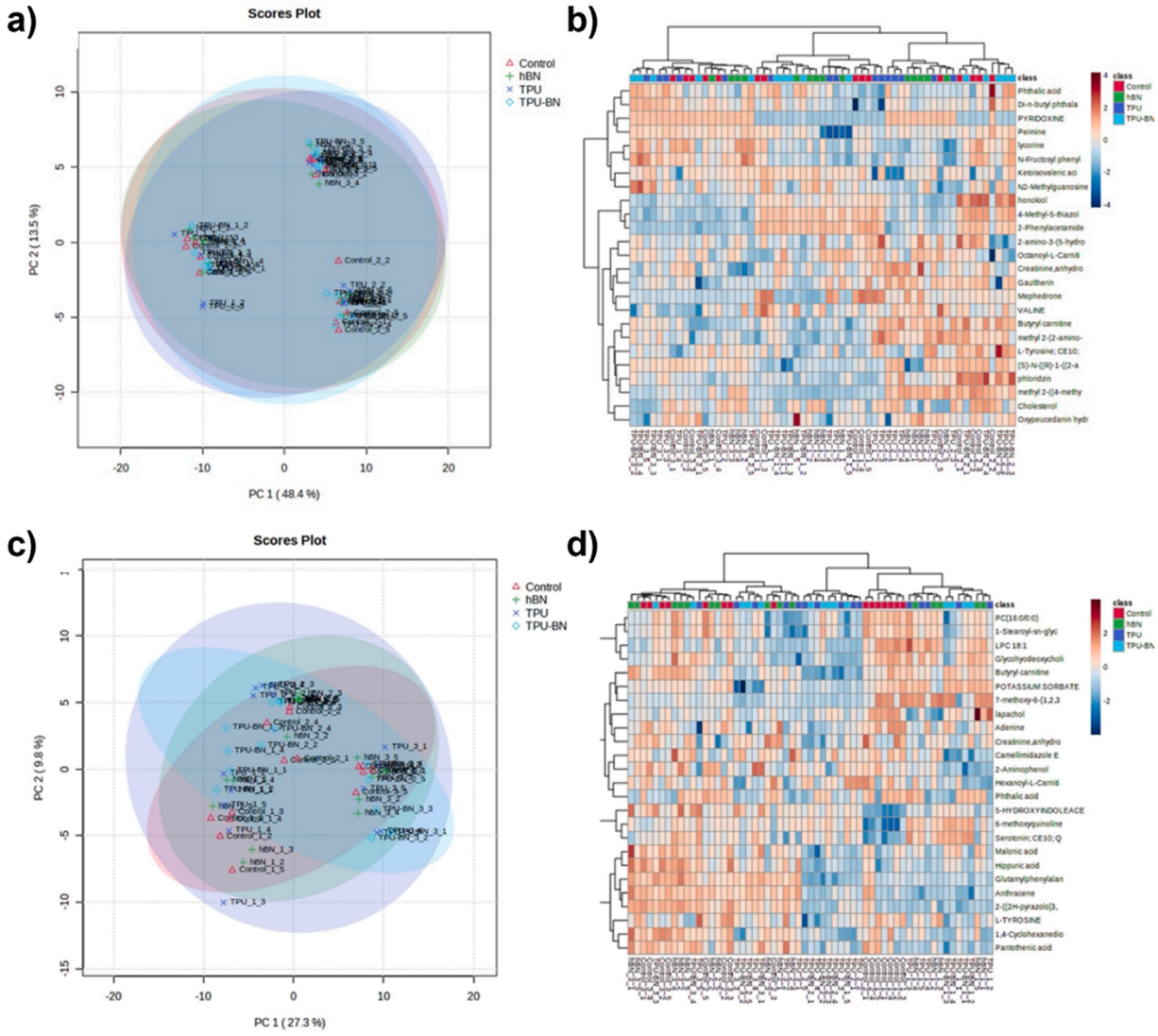

Fig. 11. PCA scores plot (a,c) and heatmap analysis (b,d) of the secretomics data acquired on HaCaT cell model, following 24 h exposure (a,b) or chronic exposure (c, d) to hBN, TPU and TPU-hBN.

cells. Protein phosphorylation is one of the most important regulation mechanisms that drives the cellular phenotype. We therefore evaluated protein phosphorylation levels identified in our proteomics dataset. We identified 27 DE proteins with an associated phosphorylation event in HaCaT cells following acute exposure to TPU-hBN composite. By performing a kinase enrichment analysis (KEA3) [42], we were able to identify the main drivers responsible for the phosphorylation of these proteins, namely CDK2 and EGFR (see Supplementary File 1). By performing the same enrichment for the entire list of DE proteins, we found that these two kinases were recurring hits in the top 10% of kinases which have the strongest association with the evaluated proteins for all experimental conditions. Overall, proteomics profiling upon low-dose exposures did not highlight any perturbations of pro-inflammatory signaling pathways, in line with the conventional biological assays, as reported above.

3.7.2. Secretomics of keratinocytes and bronchial cells

We also performed metabolomics on samples collected from acutely or repeatedly exposed HaCaT and BEAS-2B cells (Fig. 9). The aim was to acquire a "fingerprint" of the metabolites present in cell culture media at the end of the incubation with each material, to highlight significant alterations in the polar metabolome secreted by BEAS-2B and HaCaT cells. Surprisingly, the amount of soluble (polar) metabolites released was overall quite low, and we quantified with an acceptable confidence only around a hundred of metabolites per each run, mostly amino acids and other polar compounds such as creatine, hippuric and malonic acid. Supplementary File 2 reports the data for all the quantified metabolites. This excel file reports, in separated sheets, all the metabolomics raw data from both cell lines and both exposure conditions, expressed as observed LC-MS peak areas, normalized by the internal standard (see Methods). For both cell models, a subsequent unsupervised principal component analysis (PCA) and hierarchical clustering analysis performed on all positively identified metabolites failed to highlight any significant clusterization within the samples, thus indicating that no significant differences in the secreted polar metabolome could be detected in this study (Figs. 11 and 12).

As for the proteomics experiment, no major differences in the secreted metabolome were observed in cell exposed to the different materials. Metabolomics has been successfully deployed in previous investigations of the biological impact of 2D materials. For instance, using NMR-based metabolomics, GO nanosheets were found to affect 12 metabolites in serum samples taken from mice. However, samples taken at different intervals revealed that after 21 days, the exposed groups regardless of the dose of GO were very similar to the control group,

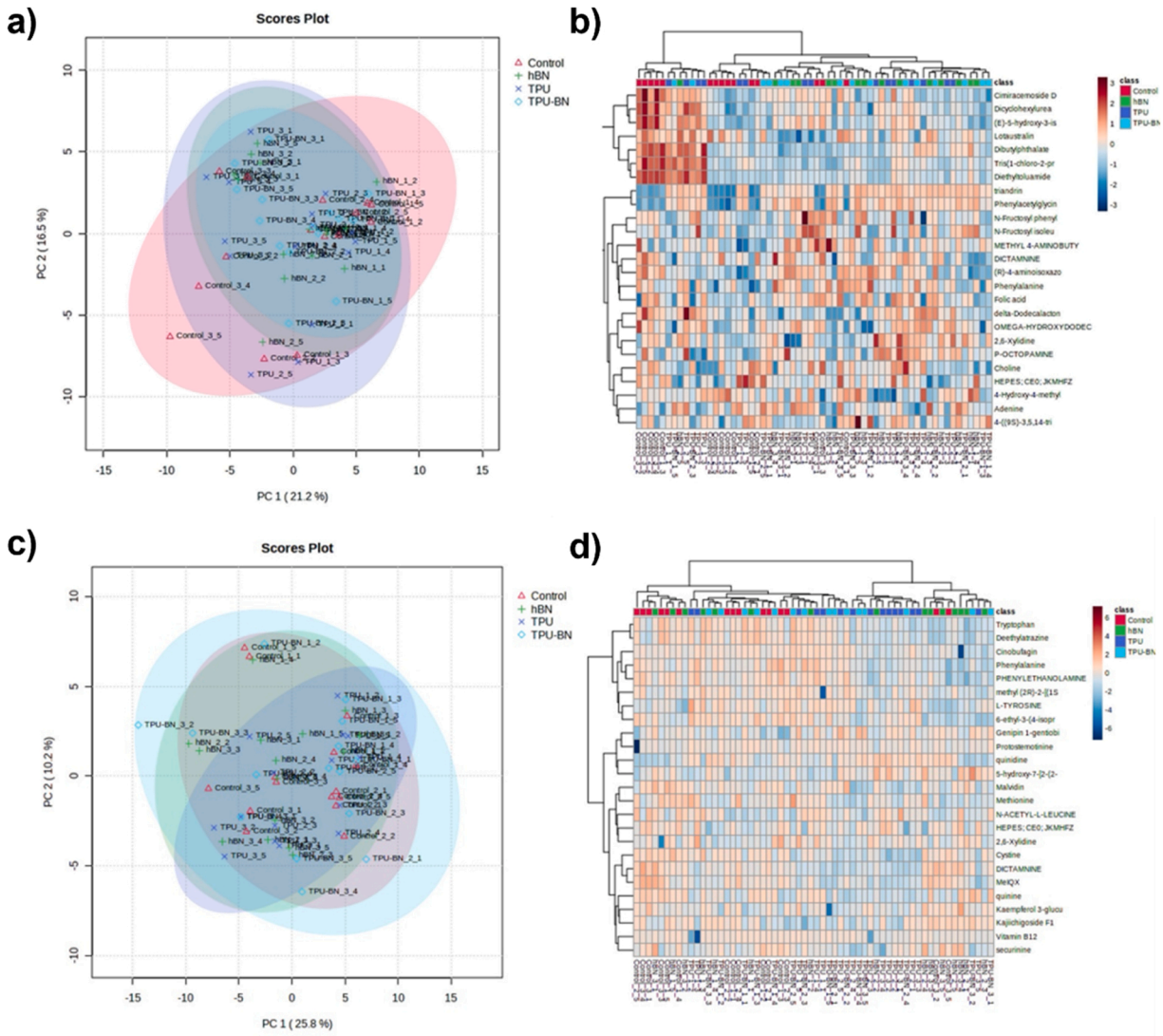

Fig. 12. PCA scores plot (a,c) and heatmap analysis (b,d) of the secretomics data acquired on BEAS-2B cell model, following 24 h exposure (a,b) or chronic exposure (c,d) to hBN, TPU and TPU-hBN.

suggesting that the toxicity of GO diminished after 21 days [80]. Furthermore, GBMs differing in their size and surface functionalization elicited different metabolic responses in the murine macrophage cell line RAW264.7 acutely exposed (24 h) at 10 μg/mL [81]. To our knowledge, only one previous study has applied metabolomics to assess the potential impact of hBN. Hence, it was shown, in a study using *Chlorella vulgaris* (a freshwater alga), that low exposure doses (0.1–1 μg/mL) of micron-sized hBN lamella triggered metabolic reprogramming, with inhibition of energy synthesis and antioxidation processes, suggesting toxicity of hBN towards photosynthetic organisms [82].

4. Conclusions

There is an urgent need to better understand the toxicological risks of nanomaterials for human health and the environment throughout the life cycle of the materials (from production to use to disposal) [83]. In a previous study on multi-walled carbon nanotubes (MWCNTs), as-produced MWCNTs were shown to elicit pulmonary inflammation in mice whereas the aerosols generated from the sanding of composites, containing MWCNTs, representative of the actual end-product, did not trigger any toxicity [84]. Moreover, in a recent study addressing reduced graphene oxide (rGO) reinforced thermoplastic composites, as-produced and abraded materials were compared with respect to their in vitro and in vivo impact, and the results showed a negligible impact of rGO-reinforced composites, whereas neat rGO was found to elicit a modest (transient) response in mouse lungs [29]. However, there are no previous studies in which as-produced and abraded composites containing hBN have been evaluated with respect to toxicity. In a very recent comparative study of hBN nanosheets and BNNTs, oropharyngeal aspiration of hBN nanosheets did not trigger pulmonary damage in mice in contrast to BNNTs, which caused a long-lasting inflammatory response in the lungs [85]. Only as-produced materials were evaluated. In contrast, in the present study we determined the potential health hazard associated with cutaneous and inhalation exposure to hBN-reinforced composites from a life cycle perspective. To this end, the study focused on TPU, a polymeric material that is known to be non-toxic under non-flammable conditions and possesses excellent elasticity and flexibility. Due to its properties, TPU has been extensively used in applications such as mobile and electronic devices casings, automotive steering wheels, footwear soles, shielding for wirings and cables [86]. TPU mechanical strength, thermal conductivity and electrical insulation properties can be enhanced by adding hBN as a filler, resulting in a commercially relevant TPU-hBN composite. The increase in mechanical properties of TPU-hBN composite could be attributed to the interfacial interactions between hBN and TPU [87]. In addition, it is

also noted that flame-retardant properties of hBN may reduce the emission of toxic isocyanates-enriched vapors under flammable conditions [86,88]. TPU-hBN was abraded using a standard approach [30], and the resulted particles were subjected to a photo-Fenton-mediated degradation to mimic the natural weathering during the life-time of such composites. Furthermore, to increase the realism of our in vitro approach, we applied two human cell lines representative of the skin and lungs, respectively, and exposed these cell lines to low doses of the materials (0.1 μg/mL and 1.0 μg/mL) twice per week up to 1 month. For comparison, cells were also exposed to the cumulative doses (0.8 and 8 μg/mL) for 24 h. We could show that the abraded TPU-hBN composites released particles exhibiting aerodynamic diameters of around 0.8–2 μm (i.e., respirable particles). Notwithstanding, conclusive evidence was provided that the particles derived from the weathering of hBN-reinforced composites were non-cytotoxic towards human skin and lung cells. Furthermore, our multi-omics analyses confirmed that there was no significant biological impact following acute or chronic (repeated) exposure, therefore elucidating the safety profile of hBN-reinforced composites from a life-cycle perspective.

Environmental implication

Beside graphene, only limited information is available about other 2D materials, such as hexagonal boron nitride (hBN). Beside the paucity of toxicological data on hBN, the hazard potential of hBN-containing products is seldom evaluated. Nevertheless, the risk for the environment, as well as for human health, could be associated not only with pristine material properties, but also with particles released after mechanical degradation during hBN-reinforced products life cycle. This study provides information on what is qualitatively and quantitatively released from an industrially-relevant hBN-reinforced composite, with careful hazard characterization from a life cycle perspective using immortalized human skin and lung cells.

CRediT authorship contribution statement

Tina Buerki-Thurnherr: Visualization, Formal analysis, Data curation. **Marija Buljan:** Supervision. **Sanjay Thorat:** Resources. **Antonio Del Rio Castillo:** Resources. **Iwona Janica:** Formal analysis. **Viviana Jehová González:** Investigation, Formal analysis, Data curation. **Savvina Chortarea:** Formal analysis. **Victor Fuster Pozo:** Formal analysis. **Aurelia Tubaro:** Data curation. **Francesco Bonaccorso:** Resources. **Dinu Ciobanu:** Writing – original draft, Investigation, Data curation. **Marco Pelin:** Writing – review & editing, Supervision, Data curation, Conceptualization. **Jasreen Kaur:** Writing – original draft, Investigation, Data curation. **Bengt Fadeel:** Writing – review & editing, Supervision, Funding acquisition, Data curation, Conceptualization. **Magnus Olsson:** Investigation. **Zhengmei Song:** Investigation. **Andrea Armirotti:** Writing – review & editing, Investigation, Formal analysis, Data curation. **Maurizio Prato:** Writing – review & editing, Project administration, Funding acquisition. **Michela Carlin:** Writing – original draft, Investigation, Data curation. **Alberto Bianco:** Writing – review & editing, Resources, Funding acquisition, Data curation, Conceptualization. **Peter Wick:** Writing – review & editing, Funding acquisition, Data curation, Conceptualization. **Ester Vazquez:** Writing – review & editing, Resources, Funding acquisition, Data curation. **Govind Gupta:** Investigation. **Tiberiu Totu:** Formal analysis, Data curation. **Guotao Peng:** Investigation, Data curation.

Declaration of Competing Interest

The authors declare the following financial interests/personal relationships which may be considered as potential competing interests: Bengt Fadeel, Alberto Bianco, Maurizio Prato, Ester Vazquez, Peter Wick reports financial support was provided by Graphene Flagship. Alberto Bianco reports financial support was provided by French National Research Agency. Ester Vazquez reports financial support was provided by European Union. If there are other authors, they declare that they have no known competing financial interests or personal relationships that could have appeared to influence the work reported in this paper.

Data availability

Data will be made available on request.

Acknowledgements

This study was supported by the European Commission through the Graphene Flagship Project (grant agreement no. 881603), the Interdisciplinary Thematic Institute SysChem, via the IdEx Unistra (ANR-10-IDEX-0002) within the French Investments for the Future Program, MCIN (PID2020–113080RB-I00) and the Junta de Comunidades de Castilla-La Mancha, with funding from the European Union's NextGenerationEU (PRTR-C17. I1-MATERIALES-PCOMPLEM). A.B. wishes to acknowledge the Centre National de la Recherche Scientifique and the Jean-Marie Lehn Foundation. The authors thank Lars Haag, EM core facility, Karolinska Institutet, for expert assistance with the TEM analysis of the nanomaterial-exposed cells, and Cathy Royer and Valérie Demais for help with TEM analyses at the "Plateforme Imagerie in vitro" at the Center of Neurochemistry (INCI, Strasbourg, France). The graphics for the Graphical Abstract and for Figs. 1 and 9 were created using BioRender.com.

Appendix A. Supporting information

Supplementary data associated with this article can be found in the online version at doi:10.1016/j.jhazmat.2024.134686.

References

[1] Liu, B., Zhou, K., 2019. Recent progress on graphene-analogous 2D nanomaterials: properties, modeling and applications. Prog Mater Sci 100, 99–169. https://doi.org/10.1016/j.pmatsci.2018.09.004.
[2] Roy, S., Zhang, X., Puthirath, A.B., Meiyazhagan, A., Bhattacharyya, S., Rahman, M.M., et al., 2021. Structure, properties and applications of two-dimensional hexagonal boron nitride. Adv Mater (Deerfield Beach, Fla) 33 (44), e2101589. https://doi.org/10.1002/adma.202101589.
[3] Wu, Z., Qi, J., Wang, W., Zeng, Z., He, Q., 2021. Emerging elemental two-dimensional materials for energy applications. J Mater Chem A 9 (35), 18793–18817. https://doi.org/10.1039/D1TA03676A.
[4] Molaei, M.J., Younas, M., Rezakazemi, M., 2021. A Comprehensive Review on Recent Advances in Two-Dimensional (2D) Hexagonal Boron Nitride. ACS Appl Electron Mater 3 (12), 5165–5187. https://doi.org/10.1021/acsaelm.1c00720.
[5] Golberg, D., Bando, Y., Huang, Y., Terao, T., Mitome, M., Tang, C., et al., 2010. Boron nitride nanotubes and nanosheets. ACS Nano 4 (6), 2979–2993. https://doi.org/10.1021/nn1006495.
[6] Ares, P., Cea, T., Holwill, M., Wang, Y.B., Roldán, R., Guinea, F., et al., 2020. Piezoelectricity in Monolayer Hexagonal Boron Nitride. Adv Mater 32 (1), 1905504. https://doi.org/10.1002/adma.201905504.
[7] Cassabois, G., Valvin, P., Gil, B., 2016. Hexagonal boron nitride is an indirect bandgap semiconductor. Article 4. Nat Photonics 10 (4) https://doi.org/10.1038/nphoton.2015.277.
[8] Song, L., Ci, L., Lu, H., Sorokin, P.B., Jin, C., Ni, J., et al., 2010. Large scale growth and characterization of atomic hexagonal boron nitride layers. Nano Lett 10 (8), 3209–3215. https://doi.org/10.1021/nl1022139.
[9] Zhang, K., Feng, Y., Wang, F., Yang, Z., Wang, J., 2017. Two dimensional hexagonal boron nitride (2D-hBN): synthesis, properties and applications. J Mater Chem C 5 (46), 11992–12022. https://doi.org/10.1039/C7TC04300G.
[10] An, L., Yu, Y., Cai, Q., Mateti, S., Li, L.H., Chen, Y.I., 2023. Hexagonal boron nitride nanosheets: preparation, heat transport property and application as thermally conductive fillers. Prog Mater Sci 138, 101154. https://doi.org/10.1016/j.pmatsci.2023.101154.
[11] Sharma, V., Kagdada, H.L., Jha, P.K., Śpiewak, P., Kurzydłowski, K.J., 2020. Thermal transport properties of boron nitride based materials: a review. Renew Sustain Energy Rev 120, 109622. https://doi.org/10.1016/j.rser.2019.109622.
[12] Datta, J., Kasprzyk, P., 2018. Thermoplastic polyurethanes derived from petrochemical or renewable resources: a comprehensive review. Polym Eng Sci 58 (S1), E14–E35. https://doi.org/10.1002/pen.24633.
[13] Gao, J., Hao, M., Wang, Y., Kong, X., Yang, B., Wang, R., et al., 2022. 3D printing boron nitride nanosheets filled thermoplastic polyurethane composites with enhanced mechanical and thermal conductive properties. Addit Manuf 56, 102897. https://doi.org/10.1016/j.addma.2022.102897.

[14] Guo, H., Niu, H., Zhao, H., Kang, L., Ren, Y., Lv, R., et al., 2022. Highly anisotropic thermal conductivity of three-dimensional printed boron nitride-filled thermoplastic polyurethane composites: effects of size, orientation, viscosity, and voids. ACS Appl Mater Interfaces 14 (12), 14568–14578. https://doi.org/10.1021/acsami.1c23944.

[15] Jia, S., Huang, L., He, Y., Qu, J.-P., 2022. Advanced thermoplastic polyurethane/hexagonal boron nitride thermal conductors via elongational flow from the aspect of experiment and simulation. Compos Part A: Appl Sci Manuf 163, 107212. https://doi.org/10.1016/j.compositesa.2022.107212.

[16] Liu, J., Li, W., Guo, Y., Zhang, H., Zhang, Z., 2019. Improved thermal conductivity of thermoplastic polyurethane via aligned boron nitride platelets assisted by 3D printing. Compos Part A: Appl Sci Manuf 120, 140–146. https://doi.org/10.1016/j.compositesa.2019.02.026.

[17] Ruan, Y., Li, N., Liu, C., Chen, L., Zhang, S., Wang, Z., 2020. Increasing heat transfer performance of thermoplastic polyurethane by constructing thermal conduction channels of ultra-thin boron nitride nanosheets and carbon nanotubes. N J Chem 44 (43), 18823–18830. https://doi.org/10.1039/D0NJ04215C.

[18] Kakarla, A.B., Kong, I., 2022. In vitro and in vivo cytotoxicity of boron nitride nanotubes: a systematic review. Article 12. Nanomaterials 12 (12) https://doi.org/10.3390/nano12122069.

[19] Kodali, V., Roberts, J.R., Glassford, E., Gill, R., Friend, S., Dunn, K.L., et al., 2022. Understanding toxicity associated with boron nitride nanotubes: Review of toxicity studies, exposure assessment at manufacturing facilities, and read-across. J Mater Res 37 (24), 4620–4638. https://doi.org/10.1557/s43578-022-00796-8.

[20] Lin, H., Peng, S., Guo, S., Ma, B., Lucherelli, M.A., Royer, C., et al., 2022. 2D Materials and primary human dendritic cells: a comparative cytotoxicity study. Small (Weinh Der Bergstr, Ger) 18 (20), e2107652. https://doi.org/10.1002/smll.202107652.

[21] Kodali, V., Kim, K.S., Roberts, J.R., Bowers, L., Wolfarth, M.G., Hubczak, J., et al., 2022. Influence of impurities from manufacturing process on the toxicity profile of boron nitride nanotubes. Small (Weinh Der Bergstr, Ger) 18 (52), e2203259. https://doi.org/10.1002/smll.202203259.

[22] Kıvanç, M., Barutca, B., Koparal, A.T., Göncü, Y., Bostancı, S.H., Ay, N., 2018. Effects of hexagonal boron nitride nanoparticles on antimicrobial and antibiofilm activities, cell viability. Mater Sci Eng C, Mater Biol Appl 91, 115–124. https://doi.org/10.1016/j.msec.2018.05.028.

[23] Şen, Ö., Emanet, M., Çulha, M., 2019. Stimulatory effect of hexagonal boron nitrides in wound healing. ACS Appl Bio Mater 2 (12), 5582–5596. https://doi.org/10.1021/acsabm.9b00669.

[24] Abdelnasir, S., Mungroo, M.R., Shahabuddin, S., Siddiqui, R., Khan, N.A., Anwar, A., 2021. Polyaniline-conjugated boron nitride nanoparticles exhibiting potent effects against pathogenic brain-eating amoebae. ACS Chem Neurosci 12 (19), 3579–3587. https://doi.org/10.1021/acschemneuro.1c00179.

[25] Mukheem, A., Shahabuddin, S., Akbar, N., Miskon, A., Muhamad Sarih, N., Sudesh, K., et al., 2019. Boron nitride doped polyhydroxyalkanoate/chitosan nanocomposite for antibacterial and biological applications. Article 4. Nanomaterials 9 (4) https://doi.org/10.3390/nano9040645.

[26] Türkez, H., Arslan, M.E., Sönmez, E., Açikyildiz, M., Tatar, A., Geyikoğlu, F., 2019. Synthesis, characterization and cytotoxicity of boron nitride nanoparticles: emphasis on toxicogenomics. Cytotechnology 71 (1), 351–361. https://doi.org/10.1007/s10616-019-00292-8.

[27] Domanico, M., Fukuto, A., Tran, L.M., Bustamante, J.-M., Edwards, P.C., Pinkerton, K.E., et al., 2022. Cytotoxicity of 2D engineered nanomaterials in pulmonary and corneal epithelium. NanoImpact 26, 100404. https://doi.org/10.1016/j.impact.2022.100404.

[28] Lucherelli, M.A., Qian, X., Weston, P., Eredia, M., Zhu, W., Samorì, P., et al., 2021. Boron nitride nanosheets can induce water channels across lipid bilayers leading to Lysosomal permeabilization. Adv Mater (Deerfield Beach, Fla) 33 (45), e2103137. https://doi.org/10.1002/adma.202103137.

[29] Chortarea, S., Kuru, O.C., Netkueakul, W., Pelin, M., Keshavan, S., Song, Z., et al., 2022. Hazard assessment of abraded thermoplastic composites reinforced with reduced graphene oxide. J Hazard Mater 435, 129053. https://doi.org/10.1016/j.jhazmat.2022.129053.

[30] Netkueakul, W., Korejwo, D., Hammer, T., Chortarea, S., Rupper, P., Braun, O., et al., 2020. Release of graphene-related materials from epoxy-based composites: characterization, quantification and hazard assessment in vitro. Nanoscale 12 (19), 10703–10722. https://doi.org/10.1039/C9NR10245K.

[31] Fadeel, B., Bussy, C., Merino, S., Vázquez, E., Flahaut, E., Mouchet, F., et al., 2018. Safety assessment of graphene-based materials: focus on human health and the environment. ACS Nano 12 (11), 10582–10620. https://doi.org/10.1021/acsnano.8b04758.

[32] Pelin, M., Sosa, S., Prato, M., Tubaro, A., 2018. Occupational exposure to graphene based nanomaterials: Risk assessment. Nanoscale 10 (34), 15894–15903. https://doi.org/10.1039/C8NR04950E.

[33] Castillo, A.E.D.R., Pellegrini, V., Ansaldo, A., Ricciardella, F., Sun, H., Marasco, L., et al., 2018. High-yield production of 2D crystals by wet-jet milling. Mater Horiz 5 (5), 890–904. https://doi.org/10.1039/C8MH00487K.

[34] Singh, B., Kaur, G., Singh, P., Singh, K., Kumar, B., Vij, A., et al., 2016. Nanostructured boron nitride with high water dispersibility for boron neutron capture therapy. Article 1. Sci Rep 6 (1) https://doi.org/10.1038/srep35535.

[35] MathWorks, I. (2020). *MATLAB, Version: 9.9. 0.*

[36] Conway, J.R., Lex, A., Gehlenborg, N., 2017. UpSetR: an R package for the visualization of intersecting sets and their properties. Bioinforma (Oxf, Engl) 33 (18), 2938–2940. https://doi.org/10.1093/bioinformatics/btx364.

[37] Kanehisa, M., Furumichi, M., Tanabe, M., Sato, Y., Morishima, K., 2017. KEGG: new perspectives on genomes, pathways, diseases and drugs. Nucleic Acids Res 45 (D1), D353–D361. https://doi.org/10.1093/nar/gkw1092.

[38] Fabregat, A., Jupe, S., Matthews, L., Sidiropoulos, K., Gillespie, M., Garapati, P., et al., 2018. The reactome pathway knowledgebase. Nucleic Acids Res 46 (D1), D649–D655. https://doi.org/10.1093/nar/gkx1132.

[39] Benjamini, Y., Hochberg, Y., 1995. Controlling the false discovery rate: a practical and powerful approach to multiple testing. J R Stat Soc: Ser B (Methodol 57 (1), 289–300. https://doi.org/10.1111/j.2517-6161.1995.tb02031.x.

[40] Core Team, R., 2022. R: a language and environment for statistical computing. R Found Stat Comput.

[41] Wu, T., Hu, E., Xu, S., Chen, M., Guo, P., Dai, Z., et al., 2021. ClusterProfiler 4.0: a universal enrichment tool for interpreting omics data. Innov (Camb (Mass)) 2 (3), 100141. https://doi.org/10.1016/j.xinn.2021.100141.

[42] Kuleshov, M.V., Xie, Z., London, A.B.K., Yang, J., Evangelista, J.E., Lachmann, A., et al., 2021. KEA3: improved kinase enrichment analysis via data integration. Nucleic Acids Res 49 (W1), W304–W316. https://doi.org/10.1093/nar/gkab359.

[43] Szklarczyk, D., Gable, A.L., Lyon, D., Junge, A., Wyder, S., Huerta-Cepas, J., et al., 2019. STRING v11: protein-protein association networks with increased coverage, supporting functional discovery in genome-wide experimental datasets. Nucleic Acids Res 47 (D1), D607–D613. https://doi.org/10.1093/nar/gky1131.

[44] Oughtred, R., Rust, J., Chang, C., Breitkreutz, B.-J., Stark, C., Willems, A., et al., 2021. The BioGRID database: a comprehensive biomedical resource of curated protein, genetic, and chemical interactions. Protein Sci: A Publ Protein Soc 30 (1), 187–200. https://doi.org/10.1002/pro.3978.

[45] Kerrien, S., Aranda, B., Breuza, L., Bridge, A., Broackes-Carter, F., Chen, C., et al., 2012. The IntAct molecular interaction database in 2012. Nucleic Acids Res 40 (Database issue), D841–D846. https://doi.org/10.1093/nar/gkr1088.

[46] Choobdar, S., Ahsen, M.E., Crawford, J., Tomasoni, M., Fang, T., Lamparter, D., et al., 2019. Assessment of network module identification across complex diseases. Nat Methods 16 (9), 843–852. https://doi.org/10.1038/s41592-019-0509-5.

[47] Tomasoni, M., Gómez, S., Crawford, J., Zhang, W., Choobdar, S., Marbach, D., et al., 2020. MONET: a toolbox integrating top-performing methods for network modularization. Bioinforma (Oxf, Engl) 36 (12), 3920–3921. https://doi.org/10.1093/bioinformatics/btaa236.

[48] Neuwirth, E., & Brewer, R.C. (2014). *ColorBrewer palettes. R package version 1.*

[49] Wickham, H., Hester, J., Francois, R., Bryan, J., Bearrows, S., & Posit, P. (2023a). Package 'readr'. Read Rectangular Text Data. https://cran.r-project.org/web/packages/readr/readr.pdf.

[50] Wickham, H., & Wickham, M.H. (2019). *Package 'stringr'*. ⟨http://stringr.tidyverse.org⟩ ⟨https://github.com/tidyverse/stringr⟩.

[51] Bolker, B., & Warnes, G. (2022). Lumley, T. gtools: Various R programming tools. R package version 3.9. 4.

[52] Murrell, P. (2014). *gridBase: Integration of base and grid graphics. R package version 0.4–7, 24.*

[53] Pedersen, T.L. (2023). Tidygraph: A tidy API for graph manipulation v1.2.3. R package version 1.

[54] Durinck, S., Spellman, P.T., Birney, E., Huber, W., 2009. Mapping identifiers for the integration of genomic datasets with the R/Bioconductor package biomaRt. Nat Protoc 4 (8), 1184–1191. https://doi.org/10.1038/nprot.2009.97.

[55] Wickham, H., Bryan, J., Posit, P., Kalicinski, M., Valery, K., Leitienne, C., & et al. (2023b). Package 'readxl'.

[56] Shikshaky, H., Ahmed, E.A., Anwar, A.M., Osama, A., Ezzeldin, S., Nasr, A., et al., 2022. A novel approach of SWATH-Based metabolomics analysis using the human metabolome database spectral library. Article 18. Int J Mol Sci 23 (18) https://doi.org/10.3390/ijms231810908.

[57] Tsugawa, H., Ikeda, K., Takahashi, M., Satoh, A., Mori, Y., Uchino, H., et al., 2020. A lipidome atlas in MS-DIAL 4. Nat Biotechnol 38 (10), 1159–1163. https://doi.org/10.1038/s41587-020-0531-2.

[58] Pang, Z., Zhou, G., Ewald, J., Chang, L., Hacariz, O., Basu, N., et al., 2022. Using MetaboAnalyst 5.0 for LC-HRMS spectra processing, multi-omics integration and covariate adjustment of global metabolomics data. Nat Protoc 17 (8), 1735–1761. https://doi.org/10.1038/s41596-022-00710-w.

[59] Mukherjee, S.P., Gupta, G., Klöditz, K., Wang, J., Rodrigues, A.F., Kostarelos, K., et al., 2020. Next-generation sequencing reveals differential responses to acute versus long-term exposures to graphene oxide in human lung cells. Small (Weinh Der Bergstr, Ger) 16 (21), e1907686. https://doi.org/10.1002/smll.201907686.

[60] Kouroupis-Agalou, K., Liscio, A., Treossi, E., Ortolani, L., Morandi, V., Pugno, N.M., et al., 2014. Fragmentation and exfoliation of 2-dimensional materials: a statistical approach. Nanoscale 6 (11), 5926–5933. https://doi.org/10.1039/C3NR06919B.

[61] Bruckmoser, K., Resch, K., 2014. Investigation of Ageing Mechanisms in Thermoplastic Polyurethanes by Means of IR and Raman Spectroscopy. Macromol Symp 339 (1), 70–83. https://doi.org/10.1002/masy.201300140.

[62] Parnell, S., Min, K., Cakmak, M., 2003. Kinetic studies of polyurethane polymerization with Raman spectroscopy. Polymer 44 (18), 5137–5144. https://doi.org/10.1016/S0032-3861(03)00468-3.

[63] Weakley, A.T., Warwick, P.C.T., Bitterwolf, T.E., Aston, D.E., 2012. Multivariate analysis of micro-raman spectra of thermoplastic polyurethane blends using principal component analysis and principal component regression. Appl Spectrosc 66 (11), 1269–1278. https://doi.org/10.1366/12-06588.

[64] de Souza, R.F.B., Maia, V.A., Zambiazzi, Priscilla, J., Otubo, L., Lazar, D.R.R., et al., 2021. Facile, clean and rapid exfoliation of boron-nitride using a non-thermal plasma process. Mater Today Adv 12, 100181. https://doi.org/10.1016/j.mtadv.2021.100181.

[65] Ali, A., Zhang, N., Santos, R.M., 2023. Mineral characterization using scanning electron microscopy (SEM): a review of the fundamentals, advancements, and

research directions. Article 23. Appl Sci 13 (23) https://doi.org/10.3390/app132312600.
[66] Oberdörster, G., Oberdörster, E., Oberdörster, J., 2005. Nanotoxicology: an emerging discipline evolving from studies of ultrafine particles. Environ Health Perspect 113 (7), 823–839. https://doi.org/10.1289/ehp.7339.
[67] Schinwald, A., Murphy, F.A., Jones, A., MacNee, W., Donaldson, K., 2012. Graphene-based nanoplatelets: a new risk to the respiratory system as a consequence of their unusual aerodynamic properties. ACS Nano 6 (1), 736–746. https://doi.org/10.1021/nn204229f.
[68] Bai, H., Jiang, W., Kotchey, G.P., Saidi, W.A., Bythell, B.J., Jarvis, J.M., et al., 2014. Insight into the mechanism of graphene oxide degradation via the Photo-Fenton reaction. J Phys Chem C, Nanomater Interfaces 118 (19), 10519–10529. https://doi.org/10.1021/jp503413s.
[69] Kurapati, R., Backes, C., Ménard-Moyon, C., Coleman, J.N., Bianco, A., 2016. White graphene undergoes peroxidase degradation. Angew Chem (Int Ed Engl) 55 (18), 5506–5511. https://doi.org/10.1002/anie.201601238.
[70] Luan, X., Martín, C., Zhang, P., Li, Q., Vacchi, I.A., Delogu, L.G., et al., 2020. Degradation of structurally defined graphene nanoribbons by myeloperoxidase and the photo-Fenton reaction. Angew Chem (Int Ed Engl) 59 (42), 18515–18521. https://doi.org/10.1002/anie.202008925.
[71] Zhou, X., Zhang, Y., Wang, C., Wu, X., Yang, Y., Zheng, B., et al., 2012. Photo-Fenton reaction of graphene oxide: a new strategy to prepare graphene quantum dots for DNA cleavage. ACS Nano 6 (8), 6592–6599. https://doi.org/10.1021/nn301629v.
[72] Kumawat, M.K., Yadav, V., Tiwari, S., Mahanta, T., Mohanty, T., 2023. Temperature controlled synthesis of boron carbon nitride nanosheets and study of their bandgap modulation and nonlinear optical properties. Carbon 214, 118363. https://doi.org/10.1016/j.carbon.2023.118363.
[73] Fusco, L., Pelin, M., Mukherjee, S., Keshavan, S., Sosa, S., Martín, C., et al., 2020. Keratinocytes are capable of selectively sensing low amounts of graphene-based materials: Implications for cutaneous applications. Carbon 159, 598–610. https://doi.org/10.1016/j.carbon.2019.12.064.
[74] Pelin, M., Lin, H., Gazzi, A., Sosa, S., Ponti, C., Ortega, A., et al., 2020. Partial reversibility of the cytotoxic effect induced by graphene-based materials in skin keratinocytes. Article 8. Nanomaterials 10 (8) https://doi.org/10.3390/nano10081602.
[75] Pelin, M., Fusco, L., León, V., Martín, C., Criado, A., Sosa, S., et al., 2017. Differential cytotoxic effects of graphene and graphene oxide on skin keratinocytes. Article 1. Sci Rep 7 (1) https://doi.org/10.1038/srep40572.
[76] Sosa, S., Tubaro, A., Carlin, M., Ponti, C., Vázquez, E., Prato, M., et al., 2023. Assessment of skin sensitization properties of few-layer graphene and graphene oxide through the Local Lymph Node Assay (OECD TG 442B). NanoImpact 29, 100448. https://doi.org/10.1016/j.impact.2022.100448.
[77] Fusco, L., Garrido, M., Martín, C., Sosa, S., Ponti, C., Centeno, A., et al., 2020. Skin irritation potential of graphene-based materials using a non-animal test. Nanoscale 12 (2), 610–622. https://doi.org/10.1039/c9nr06815e.
[78] Umrao, S., Maurya, A.K., Shukla, V., Grigoriev, A., Ahuja, R., Vinayak, M., et al., 2019. Anticarcinogenic activity of blue fluorescent hexagonal boron nitride quantum dots: as an effective enhancer for DNA cleavage activity of anticancer drug doxorubicin. Mater Today Bio 1, 100001. https://doi.org/10.1016/j.mtbio.2019.01.001.
[79] Frontiñan-Rubio, J., Llanos-González, E., González, V.J., Vázquez, E., Durán-Prado, M., 2022. Subchronic graphene exposure reshapes skin cell metabolism. J Proteome Res 21 (7), 1675–1685. https://doi.org/10.1021/acs.jproteome.2c00064.
[80] Ghiasvand Mohammadkhani, L., Khoshkam, M., Kompany-Zareh, M., Amiri, M., Ramazani, A., 2022. Metabolomics approach to study in vivo toxicity of graphene oxide nanosheets. J Appl Toxicol: JAT 42 (3), 506–515. https://doi.org/10.1002/jat.4235.
[81] Cicuéndez, M., Fernandes, M., Ayán-Varela, M., Oliveira, H., Feito, M.J., Diez-Orejas, R., et al., 2020. Macrophage inflammatory and metabolic responses to graphene-based nanomaterials differing in size and functionalization. Colloids Surf B, Biointerfaces 186, 110709. https://doi.org/10.1016/j.colsurfb.2019.110709.
[82] Zou, W., Huo, Y., Zhang, X., Jin, C., Li, X., Cao, Z., 2024. Toxicity of hexagonal boron nitride nanosheets to freshwater algae: phospholipid membrane damage and carbon assimilation inhibition. J Hazard Mater 465, 133204. https://doi.org/10.1016/j.jhazmat.2023.133204.
[83] Kim, M., Goerzen, D., Jena, P.V., Zeng, E., Pasquali, M., Meidl, R.A., et al., 2024. Human and environmental safety of carbon nanotubes across their life cycle. Article 1. Nat Rev Mater 9 (1) https://doi.org/10.1038/s41578-023-00611-8.
[84] Bishop, L., Cena, L., Orandle, M., Yanamala, N., Dahm, M.M., Birch, M.E., et al., 2017. In vivo toxicity assessment of occupational components of the carbon nanotube life cycle to provide context to potential health effects. ACS Nano 11 (9), 8849–8863. https://doi.org/10.1021/acsnano.7b03038.
[85] Visani de Luna, L.A., Loret, T., He, Y., Legnani, M., Lin, H., Galibert, A.M., et al., 2023. Pulmonary toxicity of boron nitride nanomaterials is aspect ratio dependent. ACS Nano 17 (24), 24919–24935. https://doi.org/10.1021/acsnano.3c06599.
[86] Wang, J., Zhang, D., Zhang, Y., Cai, W., Yao, C., Hu, Y., et al., 2019. Construction of multifunctional boron nitride nanosheet towards reducing toxic volatiles (CO and HCN) generation and fire hazard of thermoplastic polyurethane. J Hazard Mater 362, 482–494. https://doi.org/10.1016/j.jhazmat.2018.09.009.
[87] Ji, Z., Liu, W., Ouyang, C., Li, Y., 2021. High thermal conductivity thermoplastic polyurethane/boron nitride/liquid metal composites: the role of the liquid bridge at the filler/filler interface. Mater Adv 2 (18), 5977–5985. https://doi.org/10.1039/D1MA00637A.
[88] Yu, B., Xing, W., Guo, W., Qiu, S., Wang, X., Lo, S., et al., 2016. Thermal exfoliation of hexagonal boron nitride for effective enhancements on thermal stability, flame retardancy and smoke suppression of epoxy resin nanocomposites via sol–gel process. J Mater Chem A 4 (19), 7330–7340. https://doi.org/10.1039/C6TA01565D.